Journal of
METAMORPHIC GEOLOGY

J. metamorphic Geol., 2013, **31,** 791–812 doi:10.1111/jmg.12045

Metamorphic history of glaucophane-paragonite-zoisite eclogites from the Shanderman area, northern Iran

H. OMRANI,[1] M. MOAZZEN,[2] R. OBERHÄNSLI,[3] T. TSUJIMORI,[4] R. BOUSQUET[5] AND M. MOAYYED[2]
[1]*Department of Geology, University of Golestan, Gorgan, 49138, Iran*
[2]*Department of Geology, University of Tabriz, Tabriz, 51664, Iran (moazzen@tabrizu.ac.ir)*
[3]*Institute of Earth and Environmental Sciences, Potsdam University, Potsdam, D–14476, Germany*
[4]*Institute for Study of the Earth's Interior, Okayama University, 827 Yamada, Tottori, 682-0193, Misasa, Japan*
[5]*Institute of Geosciences, Christian-Albrechts University of Kiel, Kiel, D-24118, Germany*

ABSTRACT The Shanderman eclogites and related metamorphosed oceanic rocks mark the site of closure of the Palaeotethys ocean in northern Iran. The protolith of the eclogites was an oceanic tholeiitic basalt with MORB composition. Eclogite occurs within a serpentinite matrix, accompanied by mafic rocks resembling a dismembered ophiolite. The eclogitic mafic rocks record different stages of metamorphism during subduction and exhumation. Minerals formed during the prograde stages are preserved as inclusions in peak metamorphic garnet and omphacite. The rocks experienced blueschist facies metamorphism on their prograde path and were metamorphosed in eclogite facies at the peak of metamorphism. The peak metamorphic mineral paragenesis of the rocks is omphacite, garnet (pyrope-rich), glaucophane, paragonite, zoisite and rutile. Based on textural relations, post-peak stages can be divided into amphibolite and greenschist facies. Pressure and temperature estimates for eclogite facies minerals (peak of metamorphism) indicate 15–20 kbar at ~600 °C. The pre-peak blueschist facies assemblage yields <11 kbar and 400–460 °C. The average pressure and temperature of the post-peak amphibolite stage was 5–6 kbar, ~470 °C. The Shanderman eclogites were formed by subduction of Palaeotethys oceanic crust to a depth of no more than 75 km. Subduction was followed by collision between the Central Iran and Turan blocks, and then exhumation of the high pressure rocks in northern Iran.

Key words: eclogite; late Palaeozoic; North Iran; Palaeotethys; *P–T* path; Shanderman.

INTRODUCTION

Eclogite and blueschist facies rocks formed from oceanic crust protoliths (e.g. Agard *et al.*, 2009) along with serpentinites mark the site of subduction and closure of oceanic basins and subsequent collision to form suture zones. Eclogite and blueschist occur in many different parts of the Alpine-Himalayan orogenic belt and are mainly Cretaceous and Tertiary in age and represent the subduction of the Mesozoic Neotethys oceanic crust beneath Eurasia (e.g., Okay, 1989; Tsai & Liou, 2000; Konstantinovskaia *et al.*, 2003; Liou *et al.*, 2004; Whitney & Davis, 2006; Çetinkaplan *et al.*, 2008; Galoyan *et al.*, 2009; Yang *et al.*, 2009; Rolland *et al.*, 2009b; Okay & Whitney, 2010; Whitney *et al.*, 2011).

Older eclogite and blueschist within the Alpine-Himalayan orogen are scarce, especially at the western part of this orogen. There are not many reports of Triassic or older rocks indicating the suture of the Palaeotethys (e.g. Okay *et al.*, 2002). The Palaeotethys suture extends eastwards from Western Europe through middle Asia, northern Tibet to China and southeast Asia (Zhang *et al.*, 2008), separating regions characterized by two fundamentally different tectonic styles in the structure of the Tethysides. In Asia, regions north of the suture include northern parts of Turkey, Iran, Turkmenistan, Afghanistan, Tajikistan, Kyrgyzstan, Uzbekistan, Kazakhstan and large parts of the Russian Federation and China (Şengör, 1992) (Fig. 1).

Two main questions concerning the Palaeotethys oceanic crust and its suture are the geological evidence for the location of the suture, and the nature and direction of the Palaeotethys oceanic crust subduction. The Palaeotethys subduction system is defined mainly using volcanic, plutonic and ophiolitic rocks along the Tethysides. Some 239–222 Ma granitoids and volcanic rocks from Turkey are considered to be a result of Palaeotethys closure (Moix *et al.*, 2008). Triassic calcalkaline volcanic rocks in the Caucasus are traceable towards the east in Afghanistan, mark the Palaeotethys closure (Tikhomirov *et al.*, 2004; Gamkrelidze & Shengelia, 2007).

Carboniferous and Triassic volcanic rocks and some Devonian to Carboniferous intrusions in the

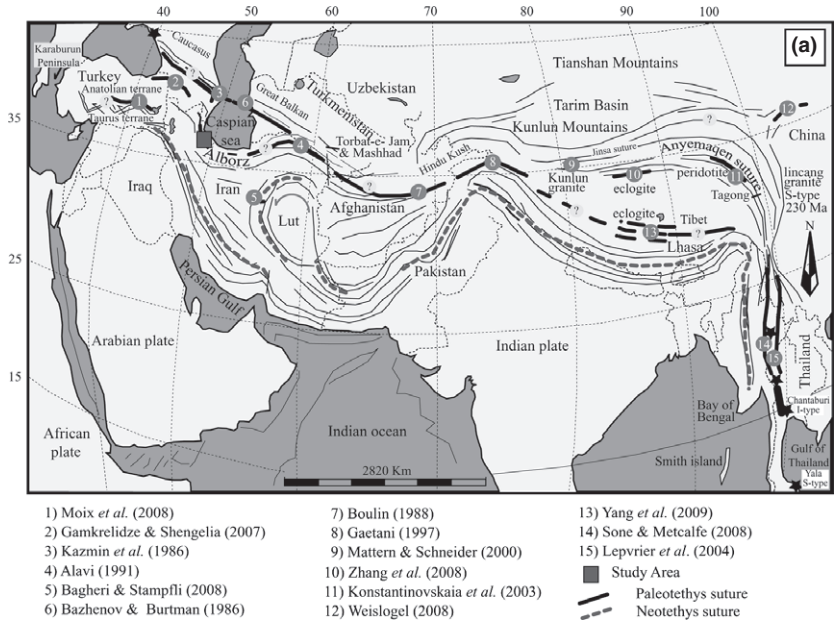

1) Moix *et al.* (2008)
2) Gamkrelidze & Shengelia (2007)
3) Kazmin *et al.* (1986)
4) Alavi (1991)
5) Bagheri & Stampfli (2008)
6) Bazhenov & Burtman (1986)
7) Boulin (1988)
8) Gaetani (1997)
9) Mattern & Schneider (2000)
10) Zhang *et al.* (2008)
11) Konstantinovskaia *et al.* (2003)
12) Weislogel (2008)
13) Yang *et al.* (2009)
14) Sone & Metcalfe (2008)
15) Lepvrier *et al.* (2004)
Study Area
Paleotethys suture
Neotethys suture

Fig. 1. (a) Palaeotethys suture from western Turkey to SE Asia. (b) Location of the study area in northern Iran and along the Alpine-Himalayan orogenic belt.

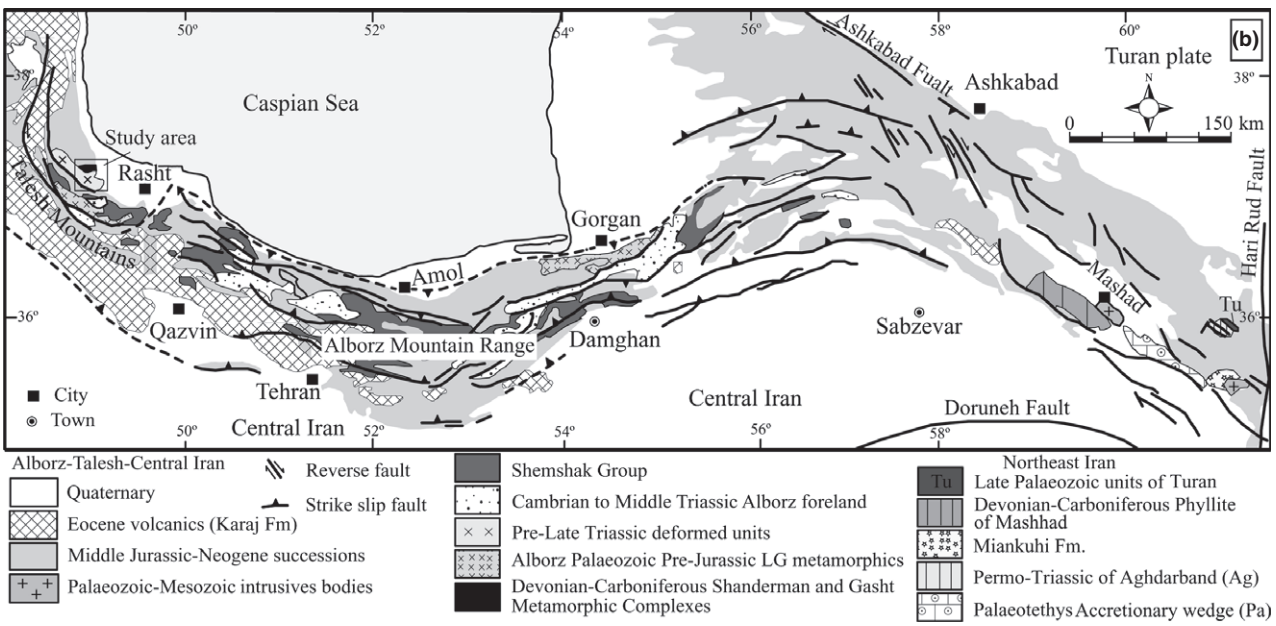

Alborz-Talesh-Central Iran
Quaternary
Eocene volcanics (Karaj Fm)
Middle Jurassic-Neogene successions
Palaeozoic-Mesozoic intrusives bodies
Reverse fault
Strike slip fault
Shemshak Group
Cambrian to Middle Triassic Alborz foreland
Pre-Late Triassic deformed units
Alborz Palaeozoic Pre-Jurassic LG metamorphics
Devonian-Carboniferous Shanderman and Gasht Metamorphic Complexes
Northeast Iran
Tu Late Palaeozoic units of Turan
Devonian-Carboniferous Phyllite of Mashhad
Miankuhi Fm.
Permo-Triassic of Aghdarband (Ag)
Palaeotethys Accretionary wedge (Pa)

southwest of Turkmenistan represent Palaeotethys-related activity to the east of the study area (Kazmin *et al.*, 1986; Lemaire *et al.*, 1997). In the northern part of Afghanistan, I-type granitoids of Hindu Kush have ages between 210 ± 10 and 112 ± 20 Ma, and S-type granitoids have been dated at 193 ± 4 Ma (Debon *et al.*, 1987). These are traceable westward into east of Iran, where the granitoids are dated at *c.* 256 to 211 ± 8 Ma (Majidi, 1978; Berberian & Berberian, 1981) and are a result of Palaeotethys subduction and subsequent collision.

Granitoids and related volcanic rocks occurring in the Karakorum area (between Pakistan, Tibet and Afghanistan; Gaetani, 1997; Mattern & Schneider, 2000; Liu *et al.*, 2004), north Tibet (Xiao *et al.,* 2007; Roger *et al.*, 2008), China (Hennig *et al.*, 2009) and Thailand (Charusiri *et al.*, 1993; Sone & Metcalfe, 2008; Kamata *et al.*, 2009) are taken as magmatic activitiy associated with subduction of the Palaeotethys oceanic basin and subsequent collision. Reports on Palaeotethys ophiolites in Asia are restricted to those from China (Zhang *et al.,* 2008) and the southern part of extensive ophiolitic exposures in Karakorum (Xu *et al.*, 1992; Zhang *et al.*, 1992; Mattern & Schneider, 2000). Eclogite and blueschist, marking the Palaeotethys suture are restricted to eclogite

(220–201 Ma) and blueschist (222–204 Ma) from the ultrahigh-pressure Qiangtang terrane, China (Kapp *et al*., 2003), eclogite from Lhasa (262 ± 5 Ma, Yang *et al.,* 2009) and blueschists from SW Japan (330–160 Ma, Nishimura, 1998).

There are different views as to the direction of subduction of oceanic crust along different segments of the Palaeotethys suture. Stampfli & Kozur (2006) believe that the Karakaya fore arc basin in Turkey formed during northward subduction of Palaeotethys oceanic crust, whereas some believe that this subduction was southward (e.g. Şengör, 1979, 1990; Jassim & Goff, 2006; Ruban *et al*., 2007). In the Caucasus, Gamkrelidze & Shengelia (2007) have proposed synchronous north and southward subduction. Furthermore, there are two ranges of granitoids in the Karakorum that are interpreted as indicating north- and southward subduction of Palaeotethys oceanic crust (Xu *et al*., 1992; Zhang *et al*., 1992; Mattern & Schneider, 2000).

This investigation of eclogite and related rocks from the Shanderman area in northern Iran adds to information on the location, subduction polarity and geodynamic evolution of the Palaeotethys suture. These Late Carboniferous (Zanchetta *et al.,* 2009) rocks are covered by Jurassic sedimentary rocks, and represent a part of the Palaeotethys suture along the Alpine-Himalayan orogen within the Alborz range of northern Iran. The Alborz range is located between the Central Iranian block to the south and the southern margin of Eurasia (Turan and south Caspian basin) to the north. The tectonics, stratigraphy and magmatism of the Alborz range have been the subject of many investigations, especially in recent years (e.g. Berberian, 1976; Kostka, 2002; Allen *et al*., 2003; Vernant *et al.,* 2004; Seyed-Emami *et al*., 2006; Zanchi *et al*., 2006; Zanchetta *et al.,* 2009). This range is divided geographically into three parts, namely Talesh, Alborz and Kopeh Dagh mountains (from west to east). The southern slope of the Alborz range is characterized by Lower to Upper Palaeozoic sedimentary rocks. Ophiolitic, metamorphic and volcanic rocks of the same age are exposed on the northern slope, whereas on the southern slope they are restricted to sites of major faults.

Some mafic and ophiolitic rocks along the Alborz range are attributed to the Palaeotethys suture zone (Stöcklin, 1974; Alavi, 1991; Dercourt *et al*., 1993; Garzanti & Gaetani, 2002; Stampfli & Borel, 2002; Natal'in & Şengör, 2005; Moazzen *et al*., 2010). The Talesh Mountains extend from the Azerbaijan Republic in the north to south of the city of Rasht in Iran. Alavi (1991) advanced the view that mafic and ultramafic rocks of the Shanderman complex are a part of the Alborz-Kopeh Dagh structural zone and connected them with the Mashhad ophiolites in NE Iran belonging to the Palaeotethys suture. Dating the Shanderman eclogites using Ar/Ar method on paragonite (Zanchetta *et al*., 2009) yielded a Late Carboniferous age (315 ± 9 Ma). Zanchetta *et al*. (2009) considered a possible Variscan Orogeny origin for the Shanderman complex and proposed that this complex is a fragment of the Upper Palaeozoic European continental crust. According to their study, this complex was stacked to the northern edge of the Iranian plate at the end of Triassic.

In this study, new geochemical, mineralogical and petrographical data are presented for the Shanderman eclogites along with documentation of the *P–T* path experienced by the rocks from subduction to exhumation, including new findings on blueschist facies metamorphism. The geochemical data and *P–T* results are in turn used to argue against a continental crust and an allochthonous origin for the studied eclogites (e.g. Zanchetta *et al*., 2009). Instead, we will show that the Shanderman eclogites were oceanic crust and mark the Palaeotethys suture in North Iran.

GEOLOGICAL BACKGROUND

The Alborz mountain range in north Iran is a result of the Cimmerian orogeny (200–150 Ma) that occurred as a result of the closure of the Palaeotethys ocean and the subsequent collision between Cimmerian blocks of Iran in the north with the southern parts of the Eurasian margin (Stampfli *et al.,* 2002). The Shanderman area is a part of the Talesh Mountains (Fig. 1a,b), which form the western part of the Alborz mountain range and flank the southwestern coast of the South Caspian Sea (Zanchetta *et al.,* 2009). The pioneering work on the geology of the Shanderman area was carried out by Clark *et al*. (1975), who called metamorphic rocks in the western part of the Alborz collectively, the Asalam-Shanderman complex.

The main rock types associated with eclogites in the Shanderman area are dunite, gabbro, greenschist, serpentinized peridotite (in some cases completely converted to serpentinite), epidote amphibolite and spilitic volcanic rocks. This rock assemblage is considered here to represent relicts of subducted oceanic crust and associated mantle. However, owing to the dismembered nature of the rock units, limited outcrops, intense weathering and dense vegetation, original igneous and tectonic contacts between these units were not found. The ultramafic rocks are serpentinized to different degrees and a serpentinite mélange is formed. The main outcrop of the eclogite-bearing serpentinite mélange appears east of Lachur village (Fig. 2). Eclogite-bearing serpentinites are emplaced either in pinkish fine-grained Jurassic limestone, or in the Shanderman complex. Eclogite-bearing serpentinites emplaced by reverse faults within these units. The contacts are not exposed. Eclogite facies rocks are found as blocks reaching up to 2 m in size in the serpentinite mélange (Fig. 3a). They appear as green rocks with relatively large (up to 1 cm) red garnet crystals (Fig. 3b).

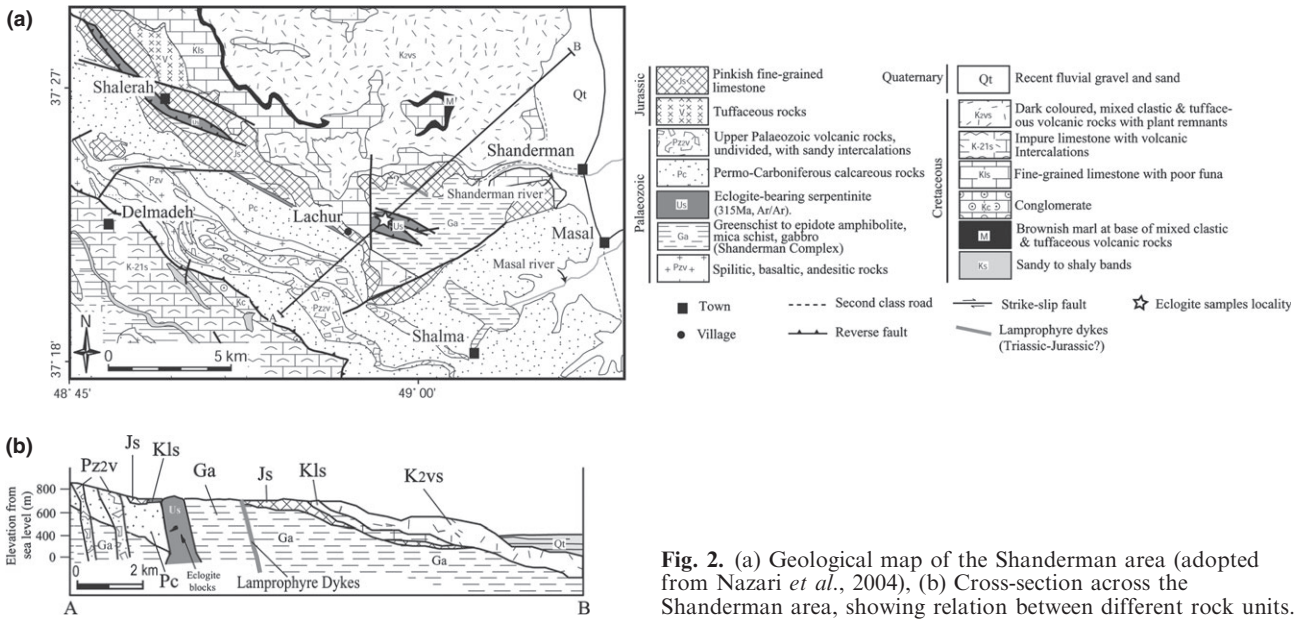

Fig. 2. (a) Geological map of the Shanderman area (adopted from Nazari *et al.*, 2004), (b) Cross-section across the Shanderman area, showing relation between different rock units.

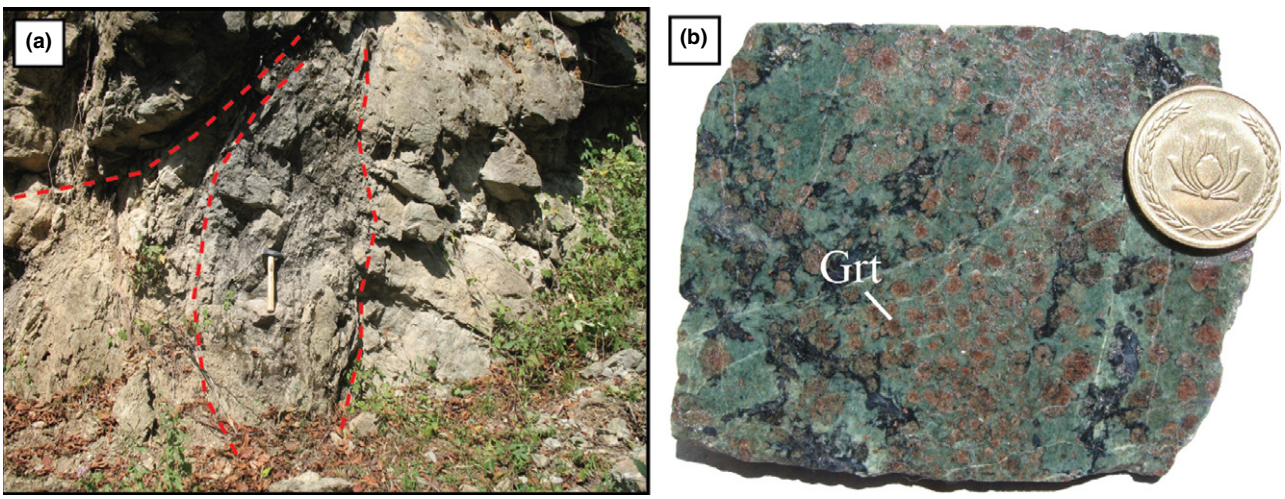

Fig. 3. (a) Outcrop of Shanderman eclogite as blocks in serpentinite, (b) polished surface of an eclogite hand specimen (Sample 100.2) showing red garnet crystals and green omphacite and amphibole.

The metamorphosed ophiolitic complex of the Shanderman area overlies basement rocks, which are mainly gneiss, micaschist and garnet-amphibolite. The best outcrop of the basement rocks is visible on the Shanderman riverside and along a forest track towards Lachur village (Fig 2). Rb-Sr dating of pelitic schists and gneiss yielded ages of 375 ± 12 and 382 ± 47 Ma, respectively, showing that the age of metamorphism of the pelites is Middle to Upper Devonian (Crawford, 1977).

The metamorphosed oceanic complex of the Shanderman area is covered by a basal conglomerate of Jurassic age (Shemshak Formation), containing serpentinite, eclogite, amphibolite and micaschist fragments. This shows that Asalam-Shanderman complex was exposed during the early Jurassic, after the Cimmerian collision.

PETROGRAPHY OF THE ECLOGITES AND SERPENTINIZED PERIDOTITES

The Shanderman eclogites can be divided into fine-grained foliated rocks (with crystals <1 mm in length) and medium to coarse-grained rocks (with crystals > 1 mm in length) with weak foliation to massive texture. Some eclogitic samples are highly retrogressed. Mineral assemblages in representative samples are provided in Table 1. Mineral name abbreviations

Table 1. Representative mineral assemblages in north Iran eclogites.

	Sample	Grt	Cpx	Amp	Rt	Ttn	Zo	Qz	Ab	Cal	Chl	Wm	Opq
1	5.38*	+	+	+	+	+	+	+	+			+	+
2	5.30	+	+	+	+	+	+	+				+	+
3	5.5	+	+	+	+	+	+	+	+			+	
4	5.39A*	+	+	+	+	+	+	+				+	
5	5.27	+	+	+	+	+	+	+	+	+	+	+	+
6	5.12	+	+	+			+	+		+		+	
7	7	+	+	+	+	+	+		+		+	+	
8	5.33	+	+	+	+	+	+		+		+	+	+
9	5.37	+	+	+	+	+	+	+				+	
10	17.1	+	+	+	+	+	+	+	+	+		+	+
11	16.9	+	+	+	+	+	+	+	+	+		+	+
12	18.2	+	+	+				+	+			+	+
13	17.2	+	+	+	+	+	+	+				+	+
14	16.10	+	+	+	+	+	+	+				+	
15	16.16*	+	+	+	+	+	+	+	+			+	
16	16.12	+	+	+	+	+	+		+			+	
17	16.2	+	+	+	+	+	+	+	+	+	+	+	
18	24.1	+	+	+	+	+	+	+				+	+
19	5.47*	+	+	+	+	+	+	+				+	
20	5.45	+	+	+	+	+	+	+	+		+	+	
21	13A	+	+	+	+	+	+	+			+	+	
21	18.3	+	+	+	+	+	+	+				+	+
22	18.6	+	+	+	+	+	+	+				+	+
23	24.2	+	+	+					+	+	+	+	
24	7.1*	+	+	+	+	+	+	+				+	
25	16.13	+	+	+	+	+	+	+	+	+	+	+	
26	5.42A	+	+	+	+	+	+		+		+	+	
27	18.10	+	+	+	+	+	+					+	
28	18.1	+	+	+	+	+	+	+				+	
29	113.5	+	+	+	+	+	+	+	+	+	+	+	+
30	119	+	+	+	+	+	+	+				+	
31	113.1	+	+	+	+	+	+	+	+	+	+	+	
32	100.2*	+	+	+	+	+	+	+	+		+	+	
33	117.1	+	+	+	+	+	+	+	+	+	+	+	

Wm, White mica.
*Analysed by EPMA.

are from Whitney & Evans (2010), unless otherwise shown.

Fine-grained eclogites

Almost all fine-grained eclogitic samples of the Shanderman area contain garnet, omphacite, rutile, amphibole, phengite, paragonite, zoisite, clinozoisite, albite, quartz and calcite. Garnet in these samples is euhedral and is wrapped by secondary hydrous phases. Garnet is zoned in two distinct parts, garnet I cores and garnet II rims. Garnet I has abundant inclusions of amphibole, rutile, titanite, quartz, white mica, albite, zoisite and clinozoisite in the core (Fig. 4a). The garnet core (Grt I) formed as pre-peak phase. Garnet II is poor in inclusions or is almost inclusion-free. It crystallized as narrow rims around garnet I (Figs 4a & 5a). Some radial fractures are visible around quartz inclusions in garnet, resembling those around coesite inclusions in garnet (e.g. O'Brien *et al.*, 2001). Omphacite is abundant in fine-grained samples, and defines a preferred orientation (foliation) along with other matrix phases. Omphacite contains rutile, quartz and glaucophane inclusions.

The fine-grained samples are divided into those with and without glaucophane. Glaucophane is zoned and rimmed by calcic amphibole. The matrix of glaucophane-free eclogites contains barrositic and tremolitic amphibole. Paragonite is abundant as a matrix phase and smaller flakes of phengite (0.5 mm) are also present (Fig. 5c). The samples contain relatively large patches of paragonite, which is partially converted to albite. Zoisite is rimmed by clinozoisite. Some zoisite crystals cut the foliation (Fig. 4b).

Medium- to coarse-grained eclogites

Garnet makes up ~30% of the modal mineralogy of these rocks. As in the fine-grained samples, garnet shows two distinct parts (Grt I and II). The inner parts of the garnet crystals (Grt I) are full of inclusions (Amp, Ep, Rt, Ph, Qz and Ttn). The outer parts (Grt II) are virtually inclusion-free. Again garnet exhibits radial cracks and parallel fractures. Radial cracks occur around some quartz inclusions (Fig . 4c). The fractures are filled by chlorite, amphibole and Fe-oxides. The shape of garnet grains is variable from idioblastic to xenoblastic. Samples rich in hydrous phases show amphibole corona textures around garnet. Omphacite, 1.5–2 mm in length (Fig. 4d), is partly converted to amphibole and albite, and contains glaucophane, rutile and quartz inclusions. All samples show high modal amounts of hydrous phases, with amphibole most prominent. Amphibole of the prograde stage is preserved in garnet and is more bluish than matrix amphibole. Fibrous amphibole in the matrix is tremolite-actinolite. White mica is typically <1 mm in size and is idioblastic. Some coarse patches of white mica seem to have crystallized earlier than other hydrous minerals. Clinozoisite and zoisite are present in all samples. In some samples, zoisite is coarse-grained (>5 mm) and contains omphacite, rutile, albite and quartz as inclusions (Figs 4e & 5b). White mica is reacted to albite at its rims, locally and contains inclusions of rutile and is mantled by inclusion-free zoisite in some samples (Fig. 4e). Rutile is commonly overgrown by titanite and occurs as inclusions in garnet, clinopyroxene, white mica, zoisite and in the matrix.

Greenschist

Greenschist is retrogressed eclogite (based on garnet composition and textural relations). It contains garnet crystals up to 2.5 mm in size, which have abundant inclusions in the core (Grt I). Narrow rims contain fewer inclusions (Grt II). Large crystals (>2.5 mm) contain green amphibole inclusions, whereas amphibole inclusions in smaller garnet are blue-green. These samples contain high amounts of colourless chlorite in the matrix (Fig. 4g). Zoisite and clinozoisite are present. Some zoisite crystals are rimmed by clinozoisite (Fig. 4b). Matrix amphibole is zoned with pale green colour in the core and blue-green at the rims (Fig. 4h). Samples of this group

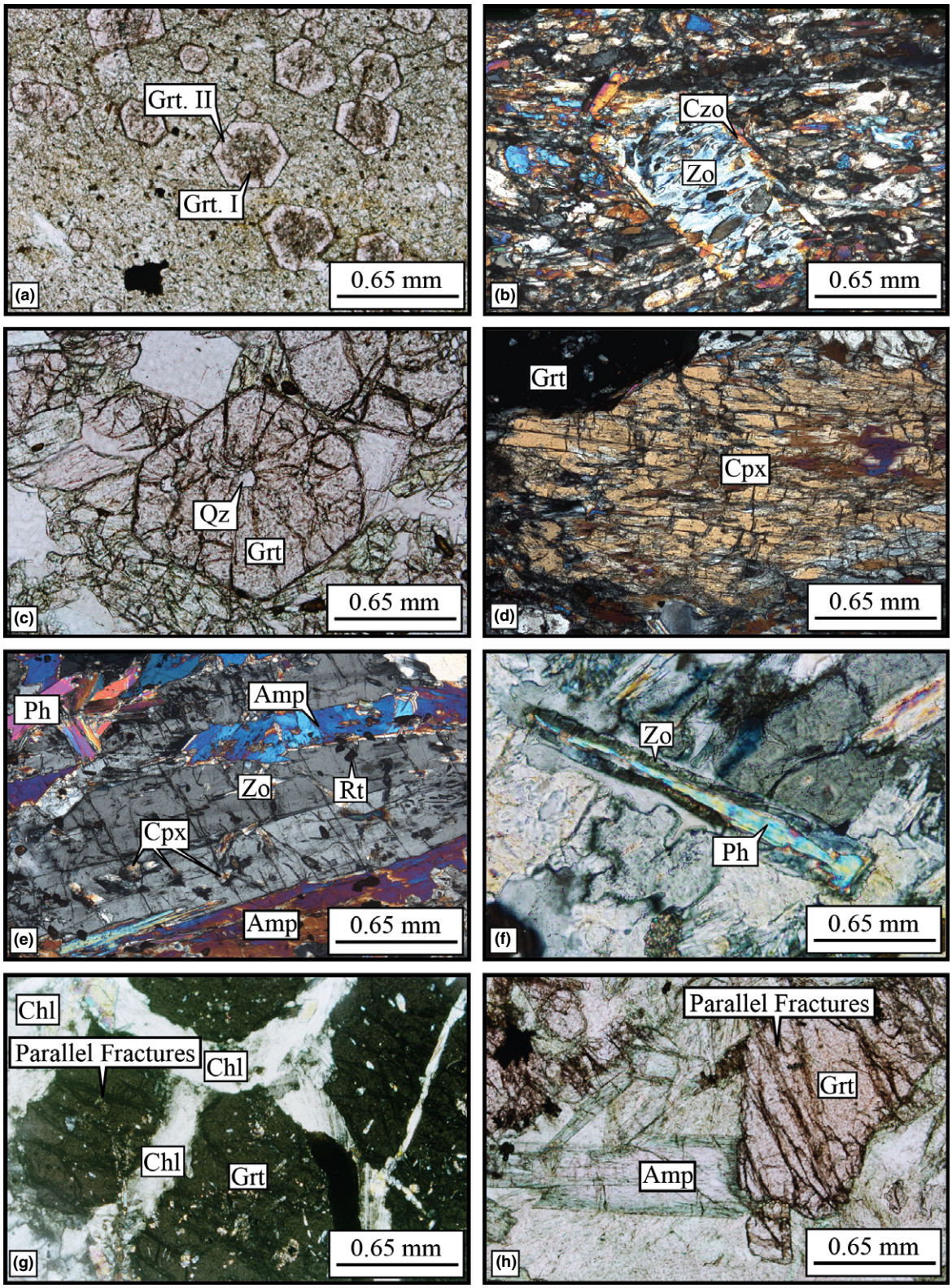

Fig. 4. Photomicrographs of Shanderman eclogite. (a) Garnet core with inclusions and rim without inclusions (Sample 5.47, PPL). (b) Zoisite rimmed by clinozoisite, cutting the rock foliation (Sample 100.2, XPL). (c) Radial cracks around quartz inclusion in garnet (Sample 5.38, PPL). D) Omphacite next to garnet (Sample, 5.39A, XPL). (e) Coarse-grained zoisite with omphacite and rutile inclusions (Sample 5.30, XPL). (f) Phengite rimmed by zoisite (Sample 5.5, XPL). (g) Parallel fractures in garnet and chlorite in the matrix (Sample 7.1, PPL). H) Zoned amphibole (Sample 7.1, PPL).

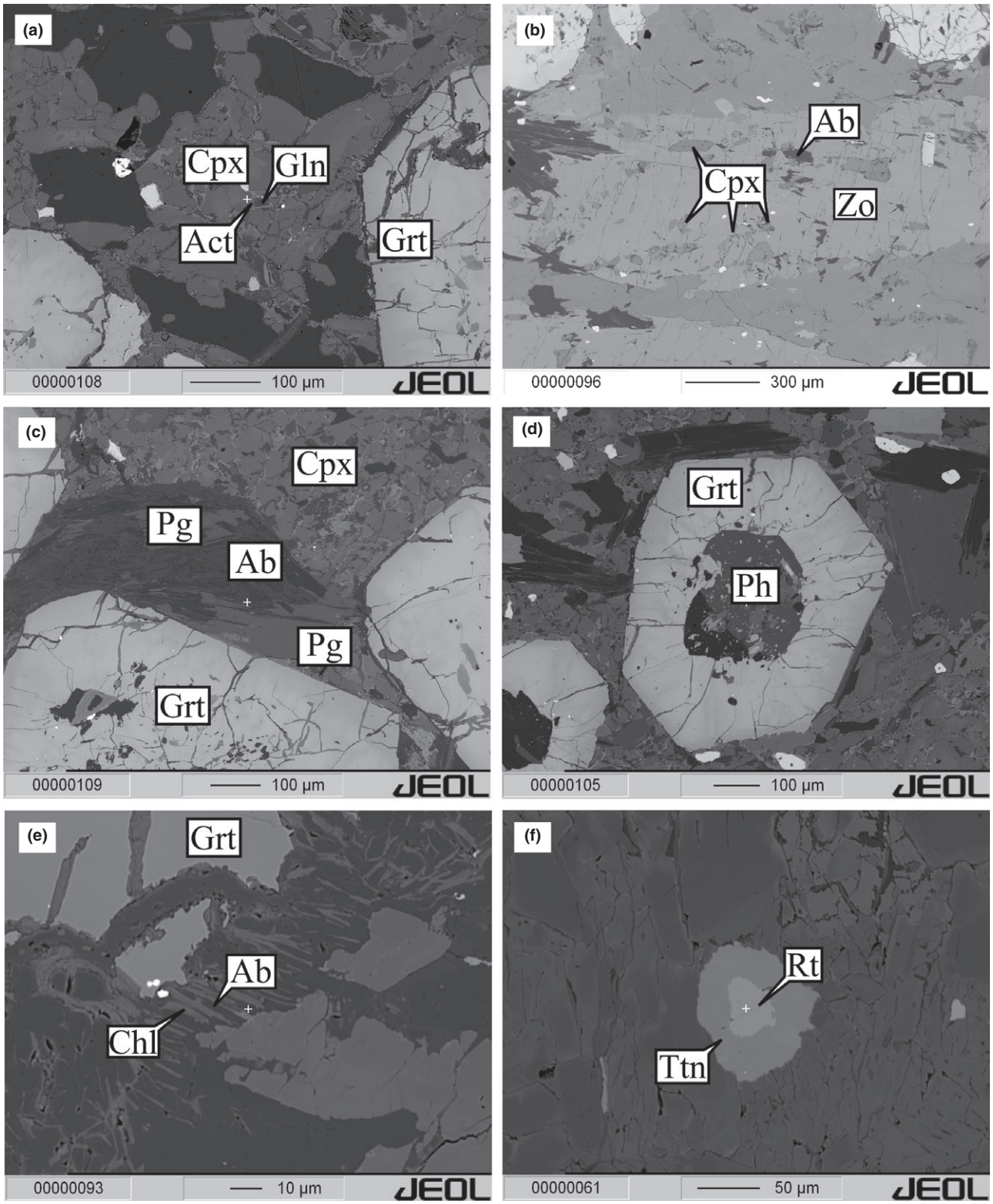

Fig. 5. Back scattered images of Shanderman eclogites. (a) actinolite riming glaucophane inclusions in omphacite, (b) omphacite and albite inclusions in zoisite, (c) paragonite changing to albite, (d) atoll garnet with phengite, (e) albite and chlorite around garnet (f) titanite around rutile.

contain no quartz in the matrix. Accessory minerals are plagioclase, opaque minerals, apatite and calcite.

Serpentinized peridotites

The studied peridotite samples are from the Shanderman valley (Fig. 2). They are composed of clinopyroxene, orthopyroxene, olivine, spinel (chromite) and serpentine. Orthopyroxene is almost entirely converted to serpentine minerals, whereas clinopyroxene and olivine are relatively fresh and converted to serpentine minerals primarily at the rims and along cracks. Clinopyroxene is rimmed by a brownish mineral that is probably clinohumite. The main rock textures are pseudomorphic (mesh, bastite and hourglass) and non-pseudomorphic (interpenetrating and interlocking). Considering the mineral assemblages, the protoliths are mainly harzburgite and to lesser extent, lherzolite. Serpentine minerals are fibrous chrysotile and lizardite.

MINERAL CHEMISTRY OF ECLOGITES

Six representative samples of eclogite were chosen for microprobe analysis. Analyses were obtained using a JEOL 8800 electron microprobe at Potsdam University, Germany, at 15 kV and 20 nA with a 2–10 μm beam. Operating conditions were 15 kV and 10–20 nA specimen current. Counting time was 10–30 s on peaks and half-peak on background. Natural and synthetic standards (Fe_2O_3[Fe], rhodonite [Mn], rutile [Ti], MgO [Mg], wollastonite [Si, Ca], fluorite [F], orthoclase [Al, K] and albite [Na]) were used for calibration.

Garnet

Zoned garnet in the Shanderman eclogites shows spessartine-rich cores, except for very small grains that seem to be a part of larger garnet cut at the crystal edges (Fig. 6). Garnet I (cores) show higher grossular and almandine and lower pyrope contents than garnet II (rims) (Table 2). Fe content increases from core to rim but at the rims shows an abrupt decrease. Two fine-grained samples, (5.38 and 100.2) contain garnet with compositions of $alm_{47\text{-}57}grs_{18–31}prp_{4–34}sps_{0–9}$ and $alm_{45–63}grs_{16–37}prp_{4–34}sps_{0–15}$ respectively. The garnet compositions in medium to coarse-grained eclogites are $alm_{47–59}grs_{23–31}prp_{6.–29}sps_{0–8}$ (sample 16.16) and $alm_{48–59}grs_{22–24}prp_{16–28}sps_{0–1}$ (sample 5.39A). X_{Mg} [=Mg/(Mg + Fe^{2+})] increases continuously from core to the rim. The lowest X_{Mg} content for Grt I is 0.08 (sample 100.2) and the highest X_{Mg} content for garnet II is 0.42 (sample 5.38) (Table 1). Small garnet has low Mn content even in the core (Fig. 6). It is rich in almandine, grossular and pyrope. For example, small garnet in sample 100.2 has a composition of $alm_{48–62}grs_{17–22}prp_{13–33}sps_{0–1}$. This shows that they correspond most likely to the outer part of larger garnet.

Table 2. Representative garnet analyses from the Shanderman eclogites.

Wt %	16.16		100.2		100.2		5.39A		5.39A		5.38	
			Small grain		Coarse grain		Coarse grain		Small grain			
	Core	Rim	Core	Rim	Core	Rim	Core	Rim	Core	Rim	Core	Rim
SiO_2	37.93	38.25	38.14	39.54	37.69	39.22	38.21	39.4	38.6	38.48	37.92	38.87
TiO_2	0.22	0.07	0.10	0.027	0.21	0.01	0.11	0.05	0.11	0.03	0.13	0.02
Al_2O_3	21.80	22.33	21.98	22.60	21.66	22.63	22.14	22.32	22.12	22.91	21.73	23.02
FeO	24.08	26.46	29.45	23.57	20.88	24.31	28.12	23.30	25.6	23.85	22.81	23.93
MnO	3.63	0.11	0.31	0.2	6.62	0.25	0.68	0.20	0.50	0.19	3.96	0.15
MgO	2.33	5.67	3.38	8.87	0.93	9.09	4.09	7.53	5.50	8.20	1.06	9.08
CaO	11.05	8.28	8.48	6.52	13.10	6.05	8.55	8.13	9.19	7.45	13.54	6.45
Na2O	0.04	0.03	0.035	0.02	0.01	0.00	0.02	0.02	0.06	0.03	0.00	0.02
K_2O	0.01	0.01	0.00	0.005	0.00	0.00	0.00	0.00	0.01	0.01	0.00	0.00
Cr_2O_3	0.00	0.18	0	0.00	0.02	0.00	0.00	0.24	0.16	0.01	0.00	0.00
Sum	101.09	101.39	101.87	101.35	101.12	101.56	101.92	101.19	101.85	101.16	101.15	101.54
Si	5.94	5.89	5.93	5.96	5.93	5.91	5.91	5.97	5.91	5.84	5.95	5.86
Ti	0.03	0.01	0.012	0.00	0.02	0.00	0.01	0.00	0.01	0.00	0.02	0.00
Al	4.02	4.05	4.02	4.01	4.02	4.02	4.03	3.99	3.99	4.10	4.02	4.09
Fe	3.15	3.41	3.82	2.97	2.75	3.06	3.63	2.95	3.28	3.03	2.99	3.01
Mn	0.48	0.01	0.04	0.02	0.88	0.03	0.08	0.02	0.06	0.02	0.53	0.02
Mg	0.54	1.30	0.78	1.99	0.22	2.04	0.94	1.70	0.12	1.85	0.25	2.04
Ca	1.85	1.37	1.41	1.05	2.21	0.97	1.41	1.32	1.51	1.21	2.28	1.04
Na	0.01	0.01	0.00	0.00	0.00	0.00	0.00	0.00	0.02	0.00	0.00	0.00
K	0.00	0.00	0.00	0.00	0.00	0.00	0.00	0.00	0.00	0.00	0.00	0.00
Cr	0.00	0.02	0.00	0.00	0.00	0.00	0.00	0.02	0.02	0.00	0.00	0.00
X_{Mg}	0.15	0.28	0.17	0.41	0.08	0.41	0.21	0.37	0.28	0.39	0.08	0.41
Alm	52.03	55.30	62.7	48.8	44.84	49.0	59.2	49.2	52.8	48.4	49.20	48.2
Prp	9.06	21.69	13.1	33.2	3.65	34.1	15.7	28.4	21	31.0	4.11	34.0
Sps	8.02	0.23	0.7	0.4	14.70	0.5	1.5	0.42	1.1	0.4	8.77	0.3
Gau	30.88	22.77	23. 5	17.6	36.81	16.3	23.6	22.0	25.2	20.2	37.92	17.4
Sum	100	100	100	100	100	100	100	100	100	100	100	100

Normalized to 24(O), X_{Mg} = Mg/(Fe^{2+}+Mg).

Clinopyroxene

Clinopyroxene in different samples have different jadeite content. The range of jadeite content in clinopyroxene from all samples analysed is 22–53.6% (Table 3; Fig. 7a,b). Peak metamorphic clinopyroxene in the matrix has a composition of $jd_{22-54}di + hd_{40-68}ae_{0-14}$ with $X_{Mg} = 0.36–0.68$. Na_2O content varies from 3.9 to 7.7 (wt%) (Table 3). The jadeite content of small omphacite inclusions in coarse (~0.7 mm) zoisite (Fig. 7b) is similar to that in matrix clinopyroxene. Its composition is $jd_{37-47.30}di + hd_{47-57}ae_{1.1-6.7}$, $X_{Mg} = 0.42–0.5$ with Na_2O content of 6.2–7.5 (wt%). The matrix omphacite is fine- to medium-grained (<1 mm up to 5 mm in size). Omphacite in sample 16.16 has the lowest jadeite content (av. 31.3%). In contrast, samples 5.47 and 5.38 show the highest jadeite contents (av. 48 and 48.6%, respectively) (Table 3). The jadeite content decreases from core to the rim, but some clinopyroxene does not show any systematic variations.

Amphibole

Amphibole is a major phase in almost all samples and displays a number of compositional and textural relations. Both relatively fresh and retrogressed eclogites contain sodic amphibole, tremolite, actinolite, tremolitic hornblende, magnesio-hornblende, pargasitic-hornblende, tschermakitic-hornblende, edenitic-hornblende and barroisite (Table 4; Figs 5a & 8). Some amphibole is zoned with pale-green cores and darker green rims (Figs 8 & 9a). Al_2O_3, Na_2O and FeO increase and MgO and SiO_2 decrease from core to the rim (Table 4; Fig. 9a–c). The Ca content of calcic amphibole ranges from 1.63 to 1.35 (p.f.u.) from core to the rim. In sample 5.39A, the Ca content (B site) increases from the core (1.67 p.f.u.) towards the rim (1.73 p.f.u.). The Na content (A site) of amphibole decreases from core to rim (0.52 to 0 p.f.u.) except for sample 5.39A (0.27 to 0.46 p.f.u.). Sodic-calcic amphibole is barroisite (as part of zoned amphibole). Alkali amphibole is glaucophane with low Ca (0.20–0.25 p.f.u.) and Al^{IV} (0.16–0.19 p.f.u.) contents (Fig. 8a). The X_{Mg} (=Mg/(Mg + Fe^{2+})) of glaucophane is 0.91–0.93 for sample 5.74 and 0.80–0.88 for sample 5.38, decreasing from core to the rim. The highest $X_{Fe^{3+}}$ (= Fe^{3+}/(Fe^{3+} + Al^{VI})) for sodic amphibole (based on stoichiometry) is 0.17 (Table 3). The $X_{Fe^{3+}}$ of prograde sodic amphibole (inclusions in garnet) is 0.18 for glaucophane and 0.44 for crossite (Table 4). The X_{Mg} of sodic amphibole from the matrix (>0.8) is higher than that for inclusions in garnet (<0.71) (Table 4; Fig. 8). Glaucophane (Amp I) inclusions (Fig. 8b) in omphacite shows lower X_{Mg} in the core in comparison with the core compositions of glaucophane (Amp II) from the matrix. This glaucophane is rimmed by actinolite (Amp IV). There is a good correlation between the decrease in FeO in garnet and its increase in glaucophane from core to the rim (Fig. 10). Omphacite does not exhibit clear zoning (Fig. 10). Sharp borders and the lack of omphacite inclusions in glaucophane, show that glaucophane was not formed by consumption of omphacite during retrogression.

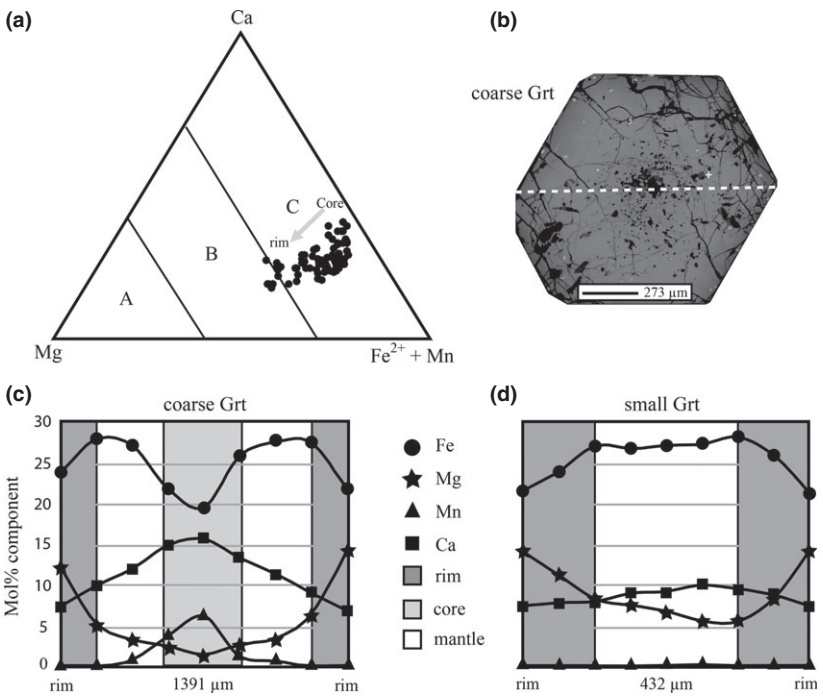

Fig. 6. (a) Ternary plots of garnet composition; (b) Back-scattered electron image of garnet in sample 100.2, the line shows microprobe traverse analyses. (c) Coarse garnet compositional zoning profiles for Ca, Mg, Mn, Fe (d) Zoning profile of small garnet in same sample (100.2).

Table 3. Representative pyroxene analyses from the Shanderman eclogites.

	In matrix										Zo*	Zo*
Wt%/sample	16.16	16.16	100.2	100.2	5.39A	5.39A	5.38	5.38	5.47	5.47	5.39	5.47
SiO_2	55.84	56.71	56.27	55.78	55.98	56.21	55.47	55.61	55.42	55.38	56.31	56.21
TiO_2	0.04	0.04	0.04	0.04	0.05	0.04	0.02	0.01	0.04	0.04	0.00	0.04
Al_2O_3	8.65	10.06	10.95	11.21	10.67	10.62	12.51	13.04	12.41	12.12	10.51	11.00
FeO	4.79	2.83	2.84	2.43	3.01	2.87	3.49	4.20	3.34	2.73	3.05	5.21
MnO	0.00	0.00	0.03	0.04	0.04	0.01	0.00	0.00	0.00	0.00	0.00	0.00
MgO	9.24	10.01	9.06	9.44	9.50	9.27	7.82	6.84	7.63	8.57	9.59	7.72
CaO	14.78	14.91	14.04	14.33	14.49	14.31	11.87	10.53	11.78	13.11	14.58	12.38
Na_2O	5.98	5.78	6.44	6.15	6.45	6.57	7.63	8.54	7.63	7.12	6.22	7.48
K_2O	0.00	0.00	0.00	0.00	0.01	0.00	0.00	0.00	0.01	0.00	0.01	0.00
Cr_2O_3	0.95	0.23	0.00	0.00	0.05	0.12	0.00	0.01	0.03	0.01	0.08	0.02
Sum	100.27	100.57	99.67	99.42	100.25	100.02	98.81	98.78	98.29	99.08	100.35	100.06
Si	1.99	2.00	2.00	1.98	1.97	1.99	1.98	1.98	1.98	1.97	1.99	1.99
Ti	0.00	0.00	0.00	0.00	0.00	0.00	0.00	0.00	0.00	0.00	0.00	0.00
Al	0.36	0.42	0.46	0.47	0.44	0.44	0.53	0.55	0.52	0.51	0.44	0.46
Fe	0.14	0.08	0.08	0.07	0.09	0.08	0.10	0.12	0.10	0.08	0.09	0.15
Mn	0.00	0.00	0.00	0.00	0.00	0.00	0.00	0.00	0.00	0.00	0.00	0.00
Mg	0.49	0.53	0.48	0.50	0.50	0.49	0.42	0.36	0.41	0.45	0.50	0.41
Ca	0.57	0.56	0.53	0.55	0.55	0.54	0.45	0.40	0.45	0.50	0.55	0.47
Na	0.41	0.40	0.44	0.42	0.44	0.45	0.53	0.59	0.53	0.49	0.43	0.51
K	0.00	0.00	0.00	0.00	0.00	0.00	0.00	0.00	0.00	0.00	0.00	0.00
Cr	0.03	0.01	0.00	0.00	0.00	0.00	0.00	0.00	0.00	0.00	0.00	0.00
X_{Mg}	0.86	0.86	0.85	0.87	0.92	0.90	0.88	0.91	0.86	0.93	0.87	0.83
Jd	35.94	40.26	44.69	43.13	40.29	42.24	48.51	50.95	49.93	45.33	41.73	44.82
Di	49.66	51.56	47.04	49.71	50.92	49.28	41.29	36.76	40.21	46.67	49.45	39.97
Hd	8.25	8.18	8.27	7.16	4.33	5.33	5.39	3.71	6.38	3.48	7.67	8.44
Ae	6.15	0.00	0.00	0.00	4.45	3.15	4.81	8.58	3.47	4.52	1.15	6.78

Normalized to 6(O), $X_{Mg} = Mg/(Fe^{2+} + Mg)$; *Zo, inclusion in Zo.

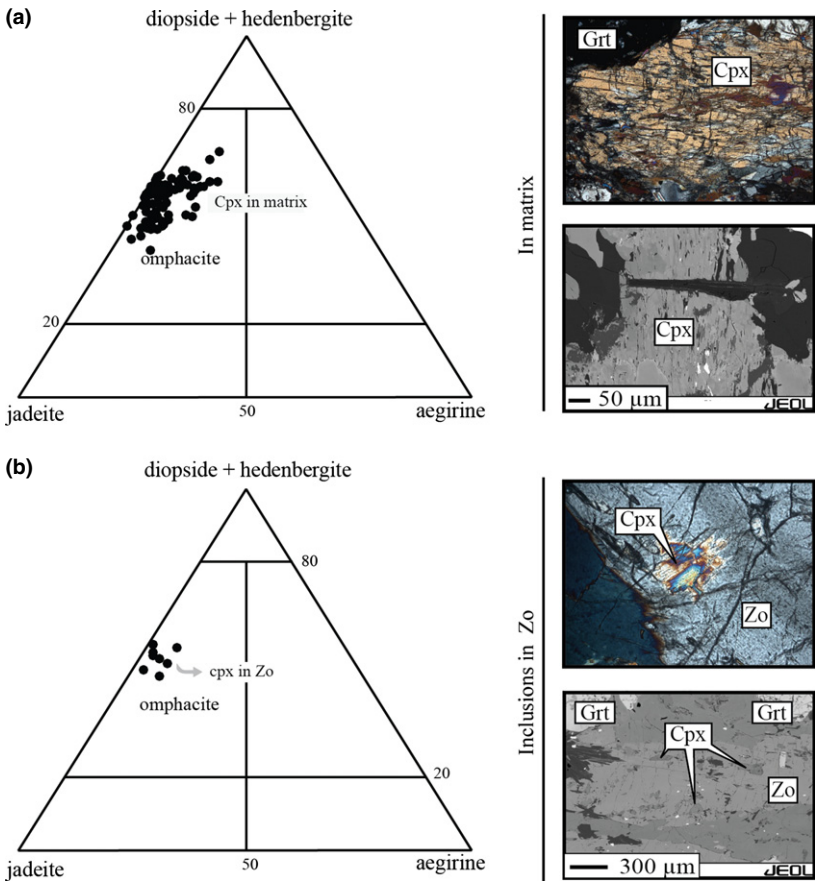

Fig. 7. (a) and (b) Ternary plots (after Morimoto *et al.*, 1988) of omphacite composition in matrix (a) and as inclusions (b); see Table 3 for sample numbers. Back-scattered electron and photomicrograph of the analysed omphacite in matrix and as inclusion in zoisite are shown.

Calcic amphibole inclusions in garnet have lower X_{Mg} than the inclusions in zoisite (>0.8). Amphibole inclusions in zoisite are characterized by Fe and Al increase and Mg and Si decrease from core to the rim. From peak amphibolite facies amphibole (Amp II) to greenschist facies amphibole (Amp IV), Al^{VI}

Table 4. Representative amphibole analyses.

Wt %	In matrix													Inclusion									
	Zoned Amp.													In Grt							In Zo	In Omph	
	16.16			7.1					5.39A		100.2	5.38	5.47	16.16	7.1					100.2	7.1	5.47	
	Act	Act-Hbl	Brs	Tr-Hbl	Mg-Hbl	Ts-Hbl	Prg-Hbl	Act	Tr	Act-Hbl	Gln	Gln	Mg-Hbl	Fprg-Hbl	Ed-Hbl	Crt	Wnc	Gln	Brs	Mg-Hbl	Mg-Hbl	Gln	Act
SiO_2	53.00	52.83	52.00	51.56	47.84	44.06	44.29	53.7	55.7	52.88	58.14	58.42	46.78	40.4	44.6	54.1	52.89	55.14	47.73	44.94	51.36	60.18	54.24
TiO_2	0.12	0.09	0.11	0.14	0.18	0.24	0.23	0.11	0.02	0.07	0.04	0.02	0.20	0.11	0.28	0.05	0.06	0.03	0.17	0.09	0.16	0.21	0.13
Al_2O_3	5.99	6.00	7.57	7.22	10.10	13.42	13.73	6.21	1.61	6.19	12.08	12.27	6.42	16.05	12.76	8.92	6.83	9.41	9.30	8.85	6.91	12.53	5.47
FeO	7.72	7.69	7.76	5.90	7.90	12.01	11.65	7.58	6.51	7.52	6.16	4.41	21.34	20.01	16.31	14.95	14.65	12.94	18.58	21.94	6.66	4.52	6.94
MnO	0.02	0.05	0.06	0.03	0.08	0.21	0.17	0.09	0.08	0.02	0.02	0.02	0.28	0.19	0.32	0.08	0.14	0.10	0.14	0.72	0.09	0.02	0.06
MgO	16.56	16.93	15.77	18.27	16.27	12.65	12.65	17.15	20.05	16.97	13.05	13.77	8.92	5.85	9.49	9.78	10.55	8.86	9.04	8.00	18.25	13.61	17.92
CaO	10.58	10.02	8.52	11.13	11.14	11.01	11.11	9.89	12.16	9.56	1.49	1.55	10.12	8.98	9.50	1.61	4.24	1.67	8.26	9.90	11.09	1.15	10.54
Na_2O	1.89	2.11	2.84	2.09	2.52	2.60	2.73	2.36	0.60	2.51	6.66	6.48	1.80	3.84	3.65	6.43	4.34	6.06	3.42	2.27	1.88	7.00	1.88
K_2O	0.05	0.06	0.06	0.23	0.27	0.24	0.24	0.10	0.02	0.11	0.02	0.02	0.03	0.06	0.15	0.03	0.04	0.02	0.03	0.06	0.21	0.02	0.09
Sum	95.92	95.80	94.69	96.58	96.33	96.47	96.79	97.21	96.76	95.85	97.70	96.96	95.88	95.49	97.06	95.92	93.73	94.23	96.69	96.76	96.61	99.25	97.27
Si	7.55	7.49	7.42	7.26	6.85	6.42	6.44	7.50	7.79	7.49	7.79	7.82	7.08	6.18	6.60	7.66	7.72	7.93	7.05	6.77	7.22	7.89	7.55
Al^{IV}	0.45	0.51	0.58	0.74	1.15	1.58	1.56	0.50	0.21	0.51	0.21	0.18	0.92	1.82	1.40	0.34	0.28	0.07	0.95	1.23	0.78	0.11	0.45
T-S	8.00	8.00	8.00	8.00	8.00	8.00	8.00	8.00	8.00	8.00	8.00	8.00	8.00	8.00	8.00	8.00	8.00	8.00	8.00	8.00	8.00	8.00	8.00
Al^{VI}	0.55	0.49	0.70	0.45	0.55	0.73	0.80	0.52	0.05	0.52	1.70	1.75	0.23	1.07	0.82	1.15	0.89	1.53	0.67	0.34	0.37	1.82	0.45
Ti	0.01	0.01	0.01	0.02	0.02	0.03	0.02	0.01	0.00	0.01	0.00	0.00	0.02	0.01	0.03	0.01	0.01	0.00	0.02	0.01	0.02	0.02	0.01
Fe^{3+}	0.12	0.36	0.45	0.29	0.39	0.57	0.44	0.34	0.35	0.37	0.34	0.29	0.83	0.63	0.44	0.92	0.81	0.33	0.63	1.00	0.49	0.14	0.30
Mg	3.51	3.58	3.36	3.83	3.47	2.75	2.74	3.57	4.18	3.58	2.60	2.75	2.01	1.33	2.09	2.06	2.29	1.90	1.99	1.80	3.82	2.66	3.72
Fe^{2+}	0.80	0.55	0.47	0.41	0.55	0.89	0.98	0.55	0.41	0.52	0.35	0.20	1.87	1.93	1.58	0.85	0.97	1.23	1.67	1.76	0.29	0.35	0.51
Mn	0.00	0.01	0.01	0.00	0.01	0.03	0.02	0.01	0.01	0.00	0.00	0.00	0.04	0.02	0.04	0.01	0.02	0.01	0.02	0.09	0.01	0.00	0.01
C-S	5.00	5.00	5.00	5.00	5.00	5.00	5.00	5.00	5.00	5.00	5.00	5.00	5.00	5.00	5.00	5.00	5.00	5.00	5.00	5.00	5.00	5.00	5.00
Ca	1.61	1.52	1.30	1.68	1.71	1.72	1.73	1.48	1.82	1.45	0.21	0.22	1.64	1.47	1.51	0.24	0.66	0.26	1.31	1.60	1.67	0.16	1.57
Na	0.39	0.48	0.70	0.32	0.29	0.28	0.27	0.52	0.16	0.55	1.73	1.68	0.36	0.53	0.49	1.76	1.23	1.69	0.69	0.40	0.33	1.78	0.43
B-S	2.00	2.00	2.00	2.00	2.00	2.00	2.00	2.00	1.98	2.00	1.94	1.90	2.00	2.00	2.00	2.00	1.89	1.95	2.00	2.00	2.00	1.94	2.00
Na	0.13	0.10	0.09	0.25	0.41	0.45	0.50	0.12	0.00	0.14	0.00	0.00	0.17	0.61	0.55	0.01	0.00	0.00	0.29	0.26	0.18	0.00	0.08
K	0.01	0.01	0.01	0.04	0.05	0.04	0.04	0.02	0.00	0.02	0.00	0.00	0.01	0.01	0.03	0.00	0.01	0.00	0.01	0.01	0.04	0.00	0.02
A-S	0.14	0.11	0.10	0.29	0.46	0.50	0.54	0.14	0.00	0.16	0.00	0.00	0.17	0.62	0.58	0.01	0.01	0.00	0.29	0.27	0.22	0.00	0.10
Xmg	0.82	0.87	0.88	0.90	0.86	0.75	0.77	0.87	0.91	0.87	0.88	0.93	0.52	0.41	0.57	0.71	0.70	0.61	0.56	0.51	0.93	0.88	0.88
XFe^{3+}											0.17	0.14				0.44		0.18				0.07	

Calculations based on 23(O), T-S, T site sum; C-A, C site sum; B-S, B site sum; A-S, A site sum. $X_{Mg} = Mg/(Fe^{2+} + Mg)$, $XFe^{3+} = Fe^{3+}/(Fe^{3+} + Al^{VI})$.

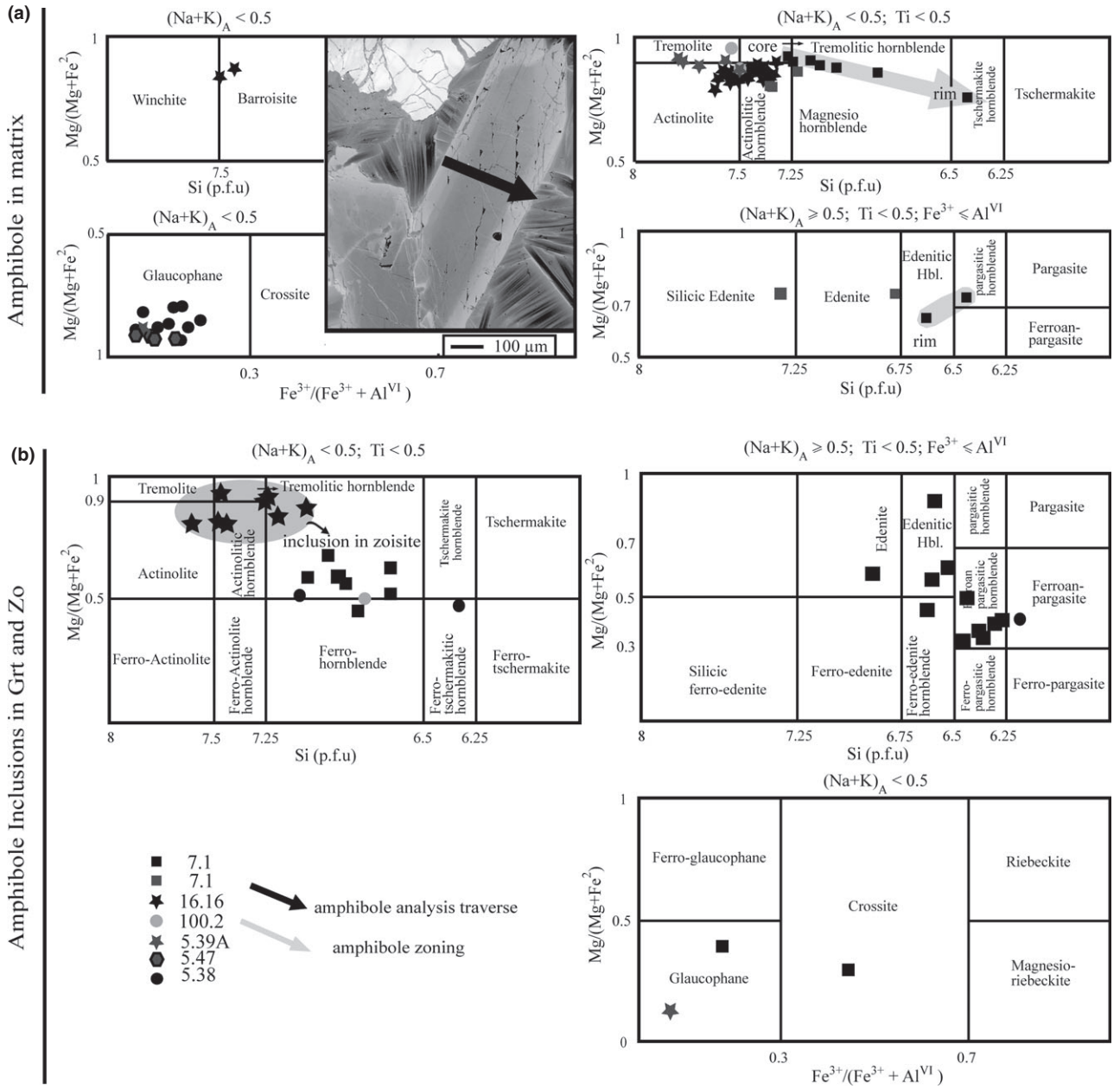

Fig. 8. Compositional variations of amphibole in Shanderman eclogites (diagram of Leake, 1978), (a) Amphibole in matrix (b) Amphibole inclusions in garnet, omphacite and zoisite.

and Na (M4) approaches its lowest values. Some zoned calcic amphibole in the matrix (sample 7.1) shows an increase in Al and Fe and a decrease in Mg contents from core to the rim (Fig. 9a-c).

Zoisite and clinozoisite

All eclogite samples contain zoisite and clinozoisite. Zoisite is more abundant than clinozoisite. It is coarse-grained (~1 cm) and contains peak metamorphic mineral inclusions (Fig. 5b). Zoisite has 0.05–0.49 Fe^{3+} (all Fe assumed to be Fe^{3+}), 2.42–2.95 Al and 1.79–2.10 Ca p.f.u. (Table 5). The Fe^{3+} content increases from core to the rim in contrast with Al and Mg contents, which decrease towards the rims (Fig. 9d–f). Al_2Fe (=100*Fe^t/(2-Al + Fe^t)) is ~26.7–54 (mol.%) and increases from core to the rim. Zoisite that is coarse-grained and aligned parallel to the foliation has lower Al_2Fe value than zoisite grains that cut foliation. The value of Al_2Fe is low (<44.8 mol.%) for zoisite and clinozoisite inclusions in garnet (Table 5).

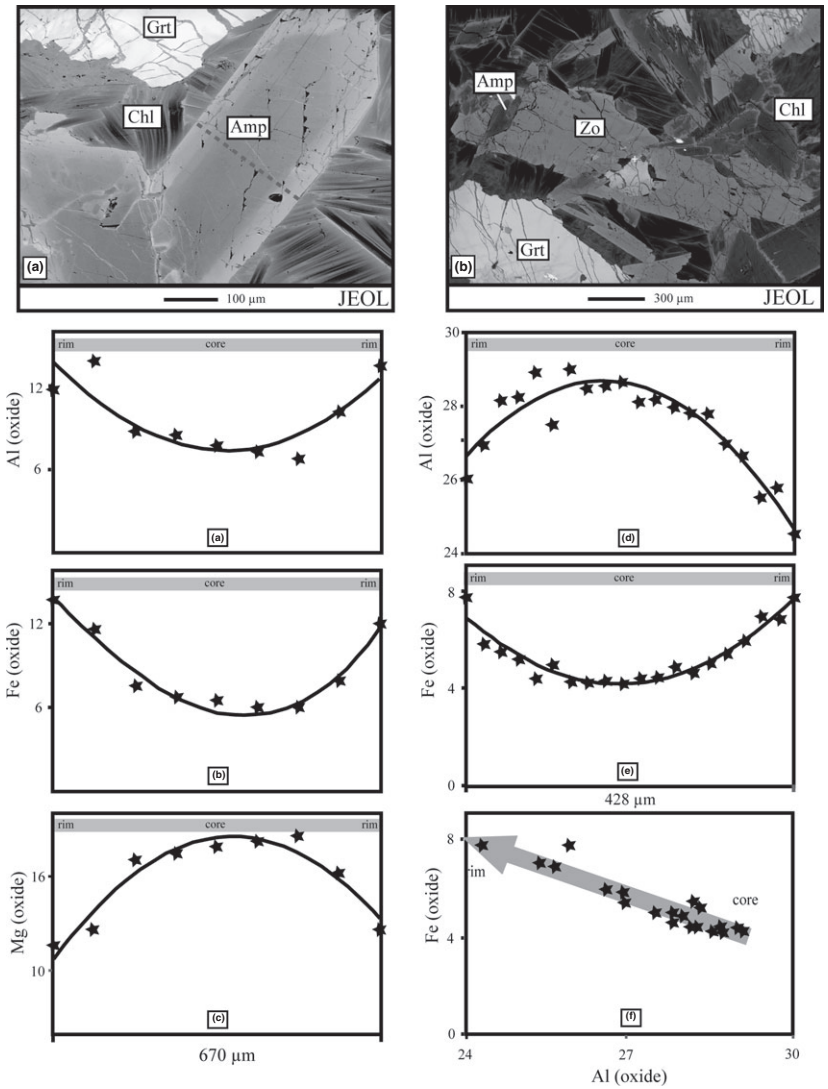

Fig. 9. Back-scatter images of amphibole and zoisite (Sample 7.1). The lines locate the microprobe traverses. (a), (b) and (c) amphibole profiles showing increasing Al and Fe contents and decreasing Mg content from core to the rim. (d) and (e) Zoisite zoning profiles show decrease of Al and increase of Fe contents from core to the rim. (f) Negative correlation of Al *v*. Fe in zoisite.

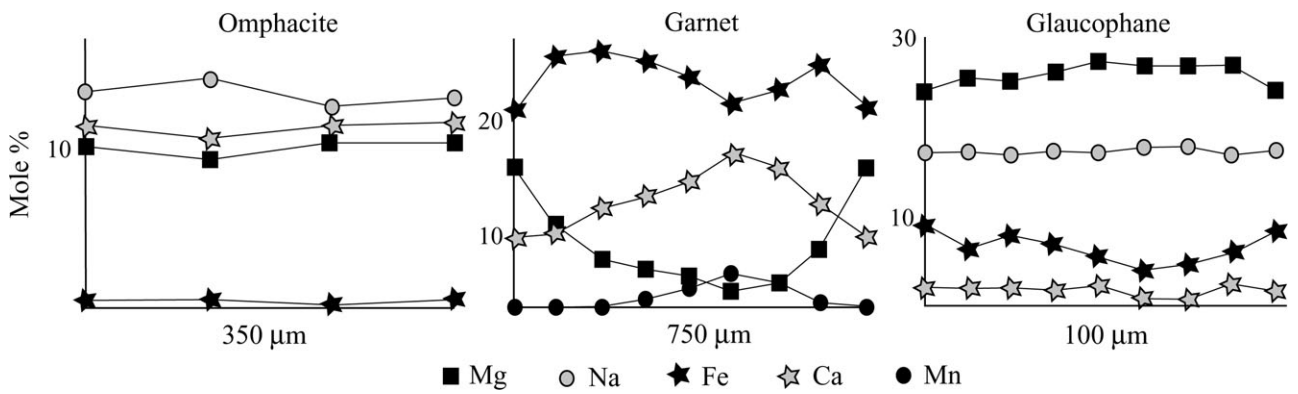

Fig. 10. Compositional zoning profiles for omphacite, garnet and glaucophane.

White mica

White mica is present in all samples. In foliated samples, mica, amphibole and epidote form the main foliation. Phengite is smaller than paragonite and has a wide range of composition (Si = 3.36–3.46 p.f.u.) (Table 5). It is zoned with higher Si in the core. Phengite has low Na/(Na + K) ratios (0.08–0.11) and high X_{Mg} that varies from 0.83 to 0.88. Phengite inclusions in garnet have Si contents of 3.42–

Table 5. Representative white micas, plagioclase, epidote minerals, ilminite and rutile analyses from the Shanderman eclogites.

Wt %	In matrix					Inclusion			Wt %	Inclusion		Wt %	In matrix			Wt %	Incl.	Wt %	In m.
						In Amp	In Grt	Atoll Grt											
	16.16	100.2	100.2	5.39A	5.47	16.16	16.16	5.47		16.16	100.2		100.2	100.2	7.1		7.1		7.1
	Pg	Pg	Ph	Pg	Ph	Pg	Pg	Ph		Ab	Ab		Zo	Czo	Czo		Ilm		Rt
SiO_2	50.75	50.15	54.119	50.49	53.53	49.21	48.09	54.13	SiO_2	67.73	71.40	SiO_2	39.69	38.56	37.78	SiO_2	0.04	SiO_2	0.03
TiO_2	0.05	0.05	0.227	0.05	0.23	0.06	0.07	0.21	TiO_2	0.024	0.04	TiO_2	0.02	0.07	0.07	TiO_2	51.44	TiO_2	96.88
Al_2O_3	40.99	40.49	28.401	41.28	30.76	40.11	40.47	29.02	Al_2O_3	19.38	20.17	Al_2O_3	31.88	28.48	26.03	Al_2O_3	0.00	Al_2O_3	0.03
FeO	0.31	0.47	1.18	0.25	0.98	0.35	0.56	1.38	FeO	0.908	0.66	FeO	1.95	6.06	7.75	FeO	41.86	FeO	2.45
MnO	0.00	0.02	0	0.01	0.00	0.00	0.00	0.01	MnO	0.105	0.07	MnO	0.01	0.03	0.12	MnO	5.18	MnO	0.12
MgO	0.44	0.32	4.366	0.14	3.76	0.11	0.09	4.07	MgO	0.045	0.01	MgO	0.02	0.14	0.02	MgO	0.04	MgO	0.00
CaO	0.30	0.27	0.03	0.29	0.05	0.32	0.61	0.02	CaO	0.412	0.54	CaO	24.87	23.87	23.91	CaO	0.43	CaO	0.58
Na_2O	3.88	5.96	0.575	6.01	0.75	6.23	6.18	0.57	Na_2O	10.77	10.64	Na_2O	0.03	0.00	0.00	Cr_2O_3	0.05	Na_2O	0.02
K_2O	0.65	1.27	9.887	0.75	9.16	0.22	0.45	9.44	K_2O	0.034	0.04	K_2O	0.00	0.00	0.00	Sum	99.04	K_2O	0.01
Sum	97.37	98.99	98.79	99.26	99.201	96.60	96.509	98.85	Sum	99.41	103.58	Sum	98.46	97.23	95.73	Si	0.00	Cr_2O_3	0.04
Si	3.11	3.07	3.44	3.07	3.37	3.07	3.02	3.43	Si	2.98	3.01	Si	3.01	3.01	3.02	Ti	1.98	Sum	100.15
Ti	0.00	0.00	0.01	0.00	0.01	0.00	0.00	0.01	Ti	0.00	0.00	Ti	0.00	0.00	0.00	Al	0.00	Si	0.00
Al	2.96	2.92	2.13	2.96	2.28	2.95	2.99	2.17	Al	1.01	1.00	Al	2.85	2.62	2.45	Fe	1.79	Ti	0.98
Fe	0.02	0.02	0.06	0.01	0.05	0.02	0.03	0.07	Fe	0.03	0.02	Fe^{3+}	0.11	0.36	0.47	Mn	0.22	Al	0.00
Mn	0.00	0.00	0.00	0.00	0.00	0.00	0.00	0.00	Mn	0.00	0.00	Mn	0.00	0.00	0.01	Mg	0.00	Fe	0.03
Mg	0.04	0.03	0.41	0.01	0.35	0.01	0.01	0.38	Mg	0.00	0.00	Mg	0.00	0.02	0.00	Ca	0.02	Mn	0.00
Ca	0.02	0.02	0.00	0.02	0.00	0.02	0.04	0.00	Ca	0.02	0.02	Ca	2.02	1.99	2.05	Cr	0.00	Mg	0.00
Na	0.46	0.71	0.07	0.71	0.09	0.75	0.75	0.07	Na	0.92	0.87	Na	0.00	0.00	0.00	Sum	4.02	Ca	0.01
K	0.05	0.10	0.80	0.06	0.73	0.02	0.04	0.76	K	0.00	0.00	K	0.00	0.00	0.00			Na	0.00
X_{Mg}	0.71	0.55	0.87	0.51	0.87	0.37	0.22	0.84	XNa	0.97	0.97	Al_2Fe	11.60	36.50	50.80			K	0.00
X_{Fe}	0.29	0.44	0.13	0.48	0.13	0.63	0.78	0.16	Xk	0.00	0.00							Cr	0.00
Mu	10	12	0.92	0.08	0.89	0.02	0.05	0.92	Xca	0.03	0.03								
Pg	90	88	0.08	0.92	0.11	0.98	0.95	0.08											

Normalizations based on 11 oxygen for mica, eight oxygen for plagioclase, 12.5 for epidote minerals, six oxygen for ilminite, two oxygen for rutile. X_{Mg} = Mg/(Mg + Fe), $X_{Fe^{3+}} = Fe^{3+}/(Fe^{3+} + Al^{VI})$, Mu = K/(Na + K), Pg = Na/(Na + K). For plagioclase, X_{Na} = Na/(Na + K + Ca), X_K = K/(K + Na + Ca), X_{Ca} = Ca/(Ca + K + Na). Al_2Fe = Fe/(−2 + Al + Fe^{3+}) (Franz & Selverstone, 1992).

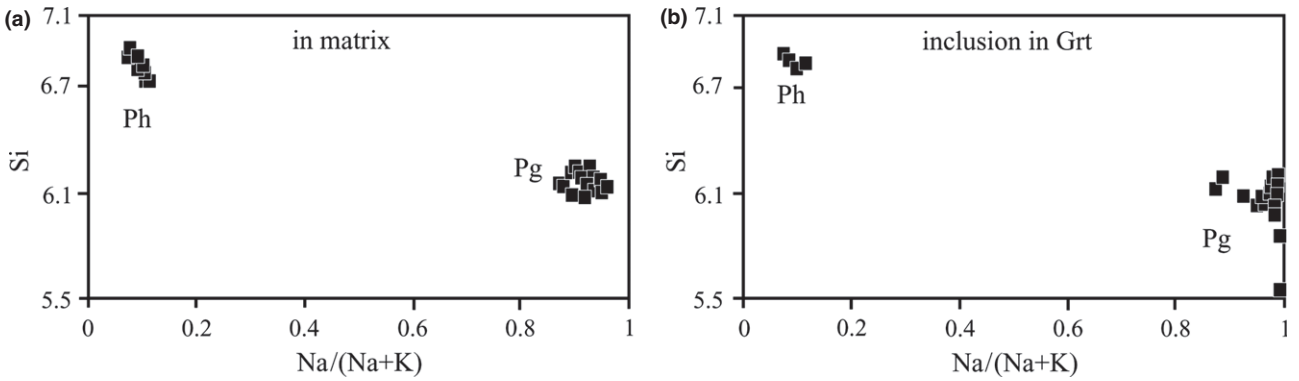

Fig. 11. Diagram of Si v. X_{Na} (p.f.u) for white mica. Samples with low X_{Na} and high Si content are phengite and the rest are paragonite. (a) White mica in matrix (b) Inclusions in garnet and amphibole.

3.45 p.f.u., X_{Mg} varies between 0.84 and 0.85 and X_{Na} from 0.07 to 0.11. The paragonite content of phengite inclusions is <11 mol.% (Table 5). Paragonite in the matrix shows low Si contents (3.05–3.12 p.f.u.), high X_{Na} (0.88–0.99 p.f.u.) and X_{Mg} (0.37–0.69 p.f.u.) (Table 5; Fig. 11). The Si content, X_{Mg} and X_{Na} decrease from core to rim. Paragonite inclusions in garnet have low Si contents, which increase from core to the rim (2.78 to 3.02 p.f.u.) (Fig. 11). Paragonite inclusions in matrix amphibole have higher Si contents than inclusions in garnet. Breakdown of paragonite produced albite (Table 5). Mg- and Fe-celadonite is a result of Mg (Fe) $Si = Al^{VI}$ Al^{IV} substitutions. When the paragonite content of phengite is high, the celadonite content is typically low. Mg-celadonite contents in phengite are up to 38 mol.%, but paragonite contents are negligible (Table 5). There are two generations of white mica: coarse patches and fine-grained. Coarse-grained white mica is paragonite that partially reacted to albite locally (Fig. 5c). Paragonite was stable at the peak of metamorphism (Fig. 5c). Small white mica grains are phengite. There are few phengite inclusions in garnet (Grt I). Phengite occurs as cores to atoll garnet in some sample (Fig. 5d).

Other minerals in eclogite

Chlorite replacing garnet in the Shanderman eclogites (Fig. 5e) is Mg-rich and does not exhibit a wide compositional range. The X_{Mg} is 0.65–0.68, Al contents are 4.78–4.90 and Si contents are 5.4–5.8 p.f.u. Albite-rich plagioclase is a secondary phase in the rocks. Some plagioclase crystals occur adjacent to paragonite and others next to omphacite. Titanite mantles rutile (Table 5). Rutile in pyrope-rich garnet rims (II) and in the matrix with a thick rim of titanite (Fig. 5f) is considered as a peak, eclogite facies phase. Quartz, calcite and iron oxides are present in the Shanderman eclogites. Zanchetta *et al.* (2009) reported aragonite from the Shanderman eclogites but it was not found in our samples.

WHOLE-ROCK CHEMISTRY OF ECLOGITES

Whole rock major and trace element analysis was undertaken on 41 Shanderman eclogite samples (Table 6). SiO_2 content varies from 39.8 to 54 wt%, clustering around 45–52 wt%, while TiO_2 is ~1 wt% and Na_2O varies from 0.37 to 5 wt%. As the major elements may change during hydrothermal alteration and high grade metamorphism, the immobile minor and trace elements have been used as protolith indicators. Trace-element discrimination diagrams (Floyd & Winchester, 1975) show a basaltic (ocean tholeiite) protolith for the Shanderman eclogites (Fig. 12a,b). Most samples fall in the MORB field of the Ti-Zr-Y and Ti-Zr-Sr plots (Fig. 12c,d), and in the normal type MORB field in the Nb-Zr-Y plot (Fig. 12e). The V content ranges between 190 and 368 ppm except for one sample with V content of 518 ppm. A TiO_2 *v.* V diagram (Shervais, 1982) shows oceanic floor basalts (Ti/V = 20–50) as likely protolith of Shanderman eclogites (Fig. 12f).

P–T CONDITIONS OF METAMORPHIC STAGES

Based on petrographic observations and microprobe analyses, prograde blueschist facies, peak eclogite facies, retrograde amphibolite facies and probable retrograde greenschist facies were recognized. The *P–T* conditions and path have been determined from the assemblages of the different stages (Fig. 13) using conventional thermobarometry and pseudosection analysis. Also mineral inclusions in different parts of the zoned garnet are used for determining *P–T* conditions of the prograde metamorphic path.

Prograde *P–T* conditions

The pre-eclogite garnet is spessartine and grossular-rich (Fig. 10), and has inclusions of prograde zoisite. Sodic, sodic-calcic and calcic amphibole formed at pre-eclogite and post-peak conditions. The presence of glaucophane (Amp I) as inclusions in garnet rims

Table 6. Representative whole-rock composition of the Shanderman eclogites. Major oxides in wt% and trace elements in ppm.

Sample	16–10	18–6	16–12	24–2	16–11	7–1	17–1	5–37	5–38	100–2
SiO_2	50.30	48.80	51.10	45.20	54.40	48.70	46.60	39.80	53.40	50.70
TiO_2	1.03	1.02	1.09	0.81	0.96	1.02	0.94	1.08	1.18	1.13
Al_2O_3	16.20	16.30	16.00	17.50	15.20	19.20	15.10	14.40	15.70	15.20
Fe_2O_3	11.52	11.35	10.56	10.05	9.39	10.11	10.12	15.16	10.68	10.84
MnO	0.16	0.28	0.11	0.23	0.17	0.19	0.14	0.39	0.13	0.18
MgO	6.57	6.06	7.16	5.79	5.67	5.72	7.71	15.13	5.89	6.77
CaO	7.16	8.02	6.21	12.45	7.25	4.85	13.03	8.70	7.34	9.58
Na_2O	4.70	3.49	4.24	3.59	4.67	2.31	2.36	0.73	3.79	3.61
K_2O	0.15	0.53	0.32	0.29	0.17	4.81	0.13	0.06	0.41	0.27
P_2O_5	0.02	0.08	0.03	0.42	0.07	0.02	0.09	0.05	0.08	0.08
LOI	2.03	3.98	2.91	3.50	1.60	2.75	3.67	4.41	1.22	1.48
Total	99.85	99.83	99.76	99.85	99.79	99.66	99.86	99.85	99.84	99.85
Ba	20	84	48	53	58	123	20	32	55	30
Cr	248	268	254	225	258	69	306	171	101	89
Ga	19	17	20	21	13	19	19	8	16	16
Nb	2	2	3	2	4	9	3	2	4	2
Ni	83	107	110	63	82	41	112	162	71	54
Rb	3	4	3	3	3	69	3	3	3	3
Sr	70	83	96	217	93	63	128	19	45	60
V	274	265	297	294	282	230	304	298	376	324
Y	27	27	24	28	23	37	25	60	29	27
Zn	86	71	88	54	72	59	72	58	25	56
Zr	66	64	69	58	68	152	63	72	73	71
La	9.1	12	9.1	11.5	4.1	83.1	10.6	4.8	15.5	11.4
Ce	9.9	11.5	8.5	10.9	4.8	60.3	10.3	4.6	12.5	11.4
Pr	10.4	12.1	9.4	11.6	4.2	54.7	10.5	4.5	11.4	11.9
Nd	10.9	12.8	9.9	12.3	4.8	56.5	11.5	5.4	12.5	12.9
Sm	13.8	16.8	13.1	16.6	6.2	33.8	14.7	12.8	14.8	16.1
Eu	13.9	17.5	14.2	21.6	5.9	25.9	16.6	25.8	14.9	16.9
Gd	15.6	18	15.1	18.2	6.8	31.3	16.3	28.0	16.6	17.7
Tb	18.1	19.3	15.9	18.2	8.8	31.8	17.4	31.8	18.5	16.2
Dy	16.8	18.5	16.0	16.4	6.6	25.6	16.1	35.1	18.3	17.9
Ho	16.3	18.2	15.9	16.3	6.1	23.0	15.9	36.6	17.7	16.9
Er	17.2	19.1	16.8	17.3	6.7	23.3	16.7	41.0	18.8	17.9
Tm	16.4	18.1	16.3	16.5	6.4	22.3	15.6	40.3	19.0	17.2
Yb	16.4	18.5	16.7	16.9	6.4	22.6	16.0	43.7	18.5	17.4
Lu	16.2	18.6	16.9	17.0	6.6	22.9	16.0	44.1	18.6	17.5
Sc	39.7	41	41.3	33.6	19.4	22	39.7	46.9	33.9	40.1

and omphacite, as well as in the matrix, shows that the Shanderman eclogites experienced blueschist facies conditions during prograde metamorphism. Rutile inclusions in garnet cores are attributed to the pre-eclogite stage. Minerals such as amphibole (sodic, sodic-calcic and calcic), quartz, white mica, albite, ilmenite, epidote, rutile, titanite and ± chlorite are preserved as inclusion in garnet. The absence of sodic pyroxene at this stage indicates a pressure below 11 kbar at 400–550 °C (Fig. 14a). The presence of titanite with rutile at pre-peak conditions indicates a wide temperature range. The *P–T* condition of the prograde blueschist stage is restricted to the albite stability field in the high temperature portion of the epidote blueschist facies. Considering the garnet cores, the maximum temperature is limited by the garnet producing reaction, with increasing temperature within a pressure range 6–11 kbar. That sets an upper temperature limit for the prograde assemblage of ~450–500 °C (e.g. Maruyama *et al.*, 1986; Evans, 1990; Okay *et al.*, 1998).

Peak *P–T* conditions

Pyrope-rich garnet grew at the eclogite facies peak of metamorphism (Fig. 10). Zoisite was stable, as indicated by Na-rich clinopyroxene inclusions. Omphacite formed in the eclogite facies with some crystals containing inclusions of quartz, rutile, paragonite and glaucophane. Glaucophane was stable (Amp Π) in the eclogite facies (peak stage) metamorphism.

Geothermometry was carried out using garnet-clinopyroxene thermometry. The Fe^{3+} content of omphacite was calculated as $Fe^{3+} = Na(M2) + (Al^{IV}(Al^{VI} + Ti))$. The calibration of Räheim & Green (1974) on four samples gave 610 °C, while the Ellis & Green (1979) calibration gave an average of 616 °C, which are higher than the 592 °C value from the Powell (1985) calibration. The calibrations of Ellis & Green (1979) and Krogh (1988) yielded 642 °C and 572 °C (±100 °C) for sample (5.38), respectively. This temperature variation, apart from the nature of different calibrations, might be caused by the uncertainty in the estimation of the Fe^{2+}/Fe^{3+} ratio of omphacite (e.g. Tsujimori *et al.,* 2006). Estimated pressures using the jadeite content of omphacite (Holland, 1979, 1980, 1983) are 13–15 kbar (Fig. 14a), while the jadeite content of omphacite inclusions in zoisite (Holland, 1979, 1980, 1983) gives 15 kbar (uncertainty <2 kbar). Considering the absence of albite in the paragenesis, these are minimum pressures.

A pseudosection was calculated using THERIAK-DOMINO software (de Capitani & Brown, 1987)

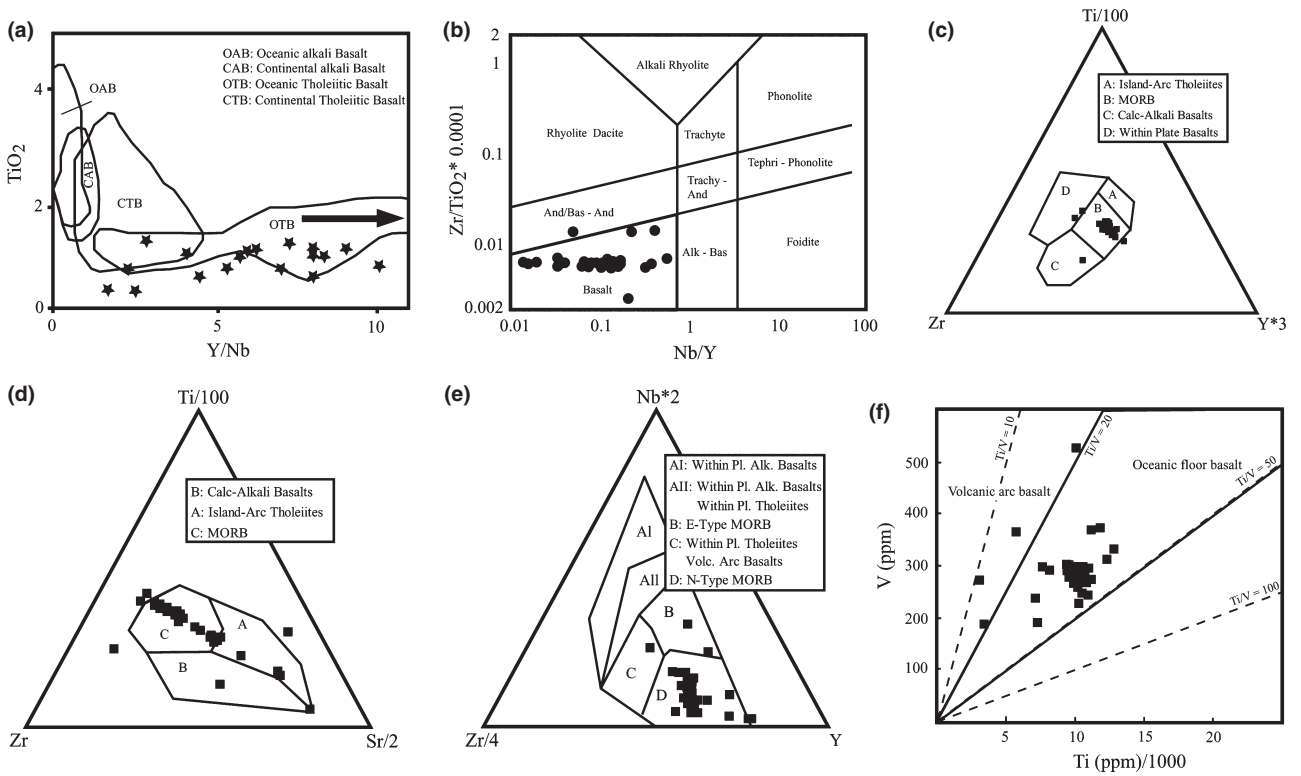

Fig. 12. Discrimination diagrams to infer protolith nature and its tectonic setting for Shanderman eclogites. The protolith was mid-oceanic ridge basalt (some data from Omrani *et al.*, 2009)

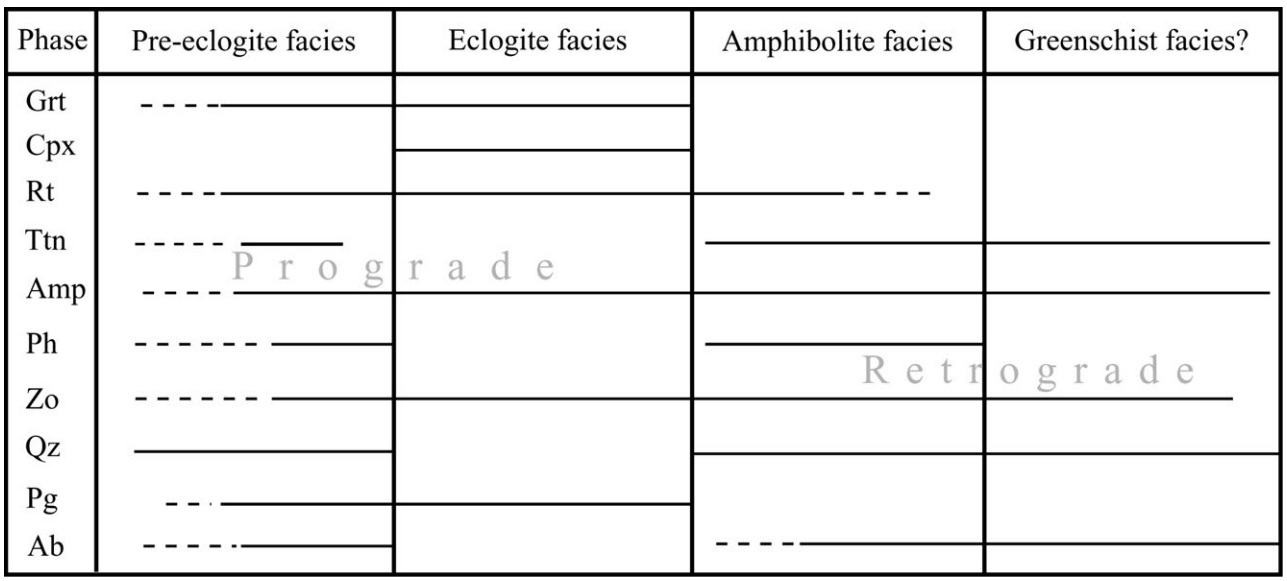

Fig. 13. Mineral assemblages for different metamorphic stages of Shanderman eclogite.

with the database of Berman (1988, updated 1992) for sample 5.38, because this sample contains the maximum number of phases in equilibrium during peak metamorphic conditions.

The pseudosection shows that peak minerals (Grt, Omp, Pg, Gln, Zo) are restricted to 13–23 kbar and 500–570 °C (Fig. 14b). The maximum pressure is defined by the stability fields of paragonite and glaucophane. Amphibole breaks down with increasing pressure at 24–25 kbar in the range 530–700 °C (Poli & Schmidt, 1995). The lower pressure of this stage is limited by the reaction Jd + Qz = Ab corresponding

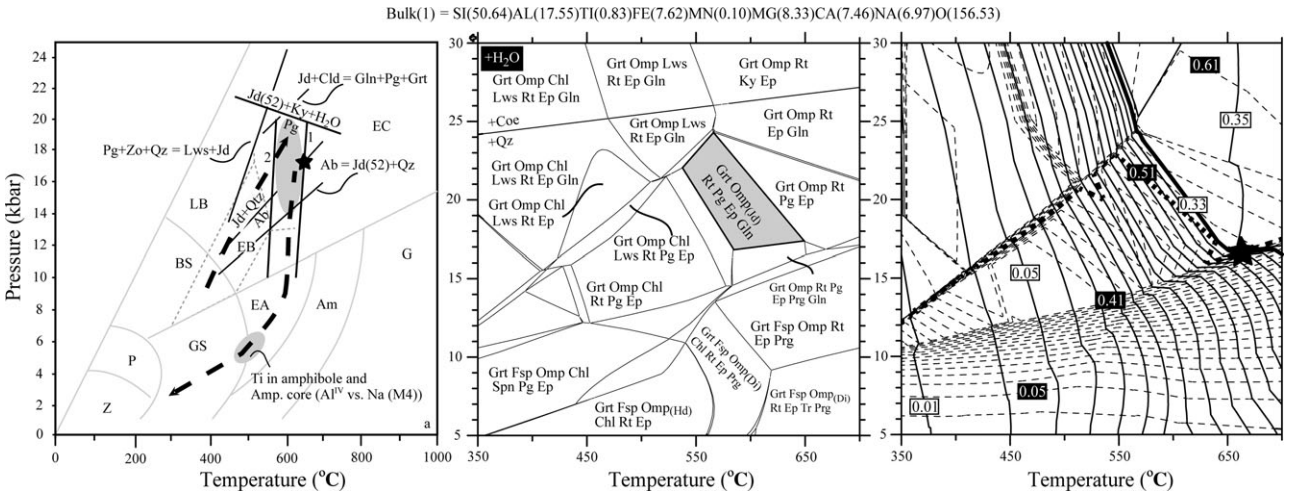

Fig. 14. (a) *P–T* diagram showing *P–T* path (dashed heavy line) for the Shanderman eclogitic rocks. The dashed grey line marks the epidote-blueschist field (EB) from Evans (1990). Black lines 1 and 2 represent garnet-clinopyroxene thermometry for sample 5.38 based on Krogh (1988) and Ellis & Green (1979) calibrations, respectively. (b) The equilibrium phase diagram for sample 5.38, calculated by the means of THERIAK-DOMINO software (de Capitani & Brown, 1987). Bulk chemistry of the sample is shown as normalized major element content. The shaded field on the diagram shows peak mineral paragenesis for the Shanderman eclogites. (c) The diagram is contoured in isopleths of X_{Jd} (clinopyroxene, black boxes), and X_{Pyp} (garnet, white boxes). The isopleths for the studied sample cross at pressure of ~16 kbar and temperature of ~650 °C (asterisk).

to 15 kbar at 600 °C. Based on jadeite content of omphacite, the maximum pressure is restricted by Pg = Jd (52) + Ky to ~20 kbar and minimum pressure ~15 kbar (Fig. 14a). The *P–T* conditions of the eclogite facies is determined from isopleths of X_{Jd}(Cpx) and X_{Pyp}(Grt), giving ~16 kbar and ~650C for the peak of metamorphism (Fig. 14c).

Post-peak *P–T* conditions

During the retrograde evolution, garnet was rimmed by amphibole. Based on textural and phase relations, some zoisite and clinozoisite formed in the epidote amphibolite and greenschist facies, after peak of metamorphism. A later generation of zoisite formed at lower amphibolite-upper greenschist facies, based on the fact that some crystals cross-cut the main foliation. Calcic-amphibole (Amp III and IV) occurs as zoned and fibrous amphibole types (Amp IV) at greenschist facies conditions. Eclogite passing through amphibolite and greenschist facies conditions during decompression is prone to retrograde reactions and formation of low *P–T* hydrous minerals. In most cases these reactions are not equilibrium reactions and therefore the exact *P–T* conditions of the retrograde path during exhumation cannot be reconstructed based on the retrograde mineral assemblages. Ambiguous textural relations among retrograde minerals add to the problem. The amphibolite stage assemblage is amphibole, plagioclase, phengite, epidote and titanite. Zoned calcic amphibole comprises tschermakitic-, edenitic and magnesio- hornblende and tremolite- and actinolitic hornblende compositions in zoned grains. Albite mole fraction in plagioclase is 0.97. The presence of hornblende in equilibrium with epidote is indicative of the epidote-amphibolite facies. Hornblende Na in M_4 site (or crossite content) barometry and Ti content thermometry on the cores of calcic amphibole reveals pressures of ~5 kbar (Brown, 1977) and temperatures of ~470 °C (Colombi, 1989). There is a slight decrease of pressure and temperature from core towards the rim. Minerals such as chlorite, zoisite, clinozoisite, albite, tremolite-actinolite, quartz and titanite indicate either greenschist facies mineral assemblages or they are products of a late pervasive alteration. Since the textural relationships between these late minerals in the retrogressed eclogites are not clear, it is not possible to define a probable local equilibrium to estimate the *P–T* condition of their formation.

Coarse phengite with quartz and epidote inclusions is visible inside atoll garnet, which probably formed during exhumation (e.g. Radvanec *et al.*, 1994; Gu *et al.*, 2002) by fluid influx. Along the retrograde path towards the greenschist facies, or by a late pervasive fluid assisted alteration, albite and chlorite developed around garnet (e.g. sample 100.2), similar to those observed by Fitzherbert *et al.* (2005).

DISCUSSION AND CONCLUSIONS

The Shanderman eclogites crop out as blocks up to two metres in size enclosed within serpentinite and serpentinised peridotite in the Talesh Mountains of the Alborz range in northern Iran. Other rock types are metabasic rocks including greenschist, epidote amphibolite and metagabbro. Eclogite-bearing serp-

entinites were emplaced by reverse faults. Although the outcrop of the eclogite-bearing serpentinites is limited in the field (Fig. 2), along with the other rock units in the area, they resemble an ophiolitic complex. Scarcity of serpentinites and metabasic blocks is a known feature for several occurrences of HP-LT metamorphic oceanic crust in the Alps-Himalaya orogen (e.g. Western Alps, Agard *et al*., 2009).

Magmatic rocks related to Palaeotethys subduction and consequent closure crop out to the north of the study area and can be taken as a possible evidence for subduction of the Palaeotethys oceanic crust in northern Iran. This gives information both on the location of the suture and direction of the subduction. The exposures of some calcalkaline intrusions in the Caucasus, west of Turkmenistan and north east of Iran can be considered as a result of Palaeotethys subduction. If this is the case, a northward subduction can be concluded for the closure of the Palaeotethys Ocean in northern Iran, in agreement with models proposed by Stampfli & Borel (2002), Stampfli & Kozur (2006) and Moix *et al*. (2008).

The Late Carboniferous-Early Permian calcalkaline intrusions and volcanism found in the Variscan Alpine-Mediterranean domain is related to the northward subduction of the Palaeotethys (Stampfli & Borel, 2002). Such magmatic activity is reported to the northwest of the Shanderman complex in the Caucasus region (Rolland *et al*., 2011). Northward subduction-related magmatism and HT-LP metamorphic rocks in southern Georgia are dated at 303 Ma (Carboniferous, Rolland *et al*., 2011). Magmatic activity and related metamorphic rocks from the Lesser Caucuses resulted from Palaeotethys (and Neotethys) northward subduction (Galoyan *et al*., 2009; Rolland *et al*., 2009a,b, 2011). However, there is no evidence for Cimmerian collision in northern Armenia, whereas evidence for such a collision is reported from Japan (Tsujimori & Itaya, 1999; Wintsch *et al.,* 1999; Tsujimori *et al.,* 2000; Tsujimori, 2002), China (Konstantinovskaia *et al*., 2003; Isozaki *et al*., 2010), Thailand (Sone & Metcalfe, 2008; Aung, 2009; Kamata *et al*., 2009), Tibet (Zhang *et al.,* 2008; Yang *et al.,* 2009), Afghanistan (Brookfield & Hashmat, 2001), Iran (Majidi, 1978; Berberian & Berberian, 1981; Zanchetta *et al.,* 2009) and Turkey (Stampfli & Kozur 2006; Moix *et al*., 2008). Considering the age of the Shanderman eclogites (315 Ma, Zanchetta *et al*., 2009) and closure time for the Palaeotethys Ocean (200–150 Ma), the Shanderman eclogites were probably exhumed early during subduction, similar to 'Group 1' exhumed subducted-oceanic crust of Agard *et al*. (2009). Whole-rock composition of the eclogites indicates that their protolith was oceanic tholeiitic basalt of MORB type generated in an oceanic floor setting.

Eclogites preserve different stages of prograde, peak and retrograde metamorphism. The presence of sodic amphibole, paragonite ± epidote minerals in garnet and clinopyroxene documents a prograde epidote blueschist facies metamorphism during subduction. Glaucophane started forming at prograde blueschist facies condition and remained stable in the eclogite facies. Omphacite + garnet in the matrix indicates eclogite facies metamorphism. At this stage pyrope-rich garnet overgrew existing garnet. The stability of hydrous phases is interpreted as reflecting high water activity at eclogite facies. The rocks have experienced late (retrograde) amphibolite and greenschist facies conditions during exhumation. This is documented by zoned calcic amphibole and chlorite in the matrix of some samples.

The estimated maximum pressure for the Shanderman eclogites is ~20 kbar and the minimum pressure is ~16 kbar. Temperatures around 554–656 °C were estimated for the metamorphic peak. The peak *P–T* conditions of the Shanderman eclogites indicate that the Palaeotethys oceanic crust was subducted to a depth of <75 km in northern Iran. During exhumation, retrograde reactions were active and produced amphibolite and greenschist facies phases. The presence of zoisite in amphibolite facies assemblage shows that the *P–T* conditions of this stage corresponded to epidote-amphibolite facies. The estimated conditions indicate a clockwise *P–T* path. The Shanderman complex is taken as a fragment of the Upper Palaeozoic European continental crust (Variscan belt, e.g. Zanchetta *et al.,* 2009), which was translated eastward during the Permian along a dextral megashear zone. In this model, the Shanderman high pressure rocks are allochthonous fragments of continental crust subducted to high depth (Zanchetta *et al.,* 2009). There is not much evidence for such a megashear zone, and there is an age difference between the eclogites (*c*. 315 Ma, Zanchetta *et al.,* 2009) and the associated gneiss and micaschist of the continental crust (*c*. 380 Ma, Crawford, 1977). Our findings show that Shanderman eclogites have oceanic lithosphere protolith and mark the location of the Palaeotethys suture in northern Iran. Petrography, mineral chemistry and *P–T* estimates show that the Shanderman eclogites were produced by subduction to a depth <75 km. This is in accordance with the typical maximum pressure estimated for subduction of oceanic crust. According to review by Agard *et al*. (2009), subducted oceanic crust rarely records pressures >20–23 kbar.

Considering the position of the Shanderman eclogites, the Palaeotethys suture zone in Iran (Alborz Mountains) is 200–500 km north of the Neotethyan suture (Zagros Mountain) and wraps around the south Caspian Sea (Axen *et al*., 2001).

ACKNOWLEDGEMENTS

This contribution is a part of the Ph.D. dissertation of the first author, which is financially supported by

University of Tabriz. We thank U. Altenberger, P. O'Brien and M. Konrad-Schmolke for their helpful discussions. Invaluable scientific comments by G. Droop are highly appreciated. We are grateful to C. Gunter and A. Musiol for their help with analysis and J. Sabouri (Geological Survey of Iran) for sharing some information on the geology of the Shanderman area. C. Fischer is acknowledged for preparing excellent thin sections. Thoughtful reviews by Y. Rolland and J. Gilotti improved the manuscript, for which we are grateful. Dr. Rolland provided us with some of his publications and unpublished data on geology of Armenia and the adjacent areas. We are grateful to D. Whitney and D. Robinson for generous help and editorial handling of the manucript.

REFERENCES

Agard, P., Yamato, P., Jolivet, L. & Burov, E., 2009. Exhumation of oceanic blueschists and eclogites in subduction zones: timing and mechanisms. *Earth Science Reviews*, **92,** 53–79.

Alavi, M., 1991. Sedimentary and structural characteristics of the Paleo-Tethys remnants in Northeastern Iran. *Geological Society of America Bulletin*, **103,** 983–992.

Allen, M.B., Ghassemi, M.R., Shahrabi, M. & Qorashi, M., 2003. Accommodation of late Cenozoic oblique shortening in the Alborz range, northern Iran. *Journal of Structural Geology*, **25,** 659–672.

Aung, H.H., 2009. Recognition of Paleo-Tethys suture zone in eastern Myanmar. *Acta Geoscience Sinica*, **30,** 1–3.

Axen, G.J., Lam, P.S., Grove, M., Stockli, D.F. & Hassanzadeh, J., 2001. Exhumation of the west-central Alborz Mountains, Iran, Caspian subsidence, and collision-related tectonics. *Geology*, **29,** 559–562.

Bagheri, S. & Stampfli, G.M., 2008. The Anarak, Jandaq and Posht-e-Badam metamorphic complexes in central Iran: new geological data, relationships and tectonic implications. *Tectonophysics*, **451,** 123–156.

Bazhenov, M.L. & Burtman, V.S., 1986. Tectonics and paleomagnetism of structural arcs of the Pamir-Punjab syntaxis. *Journal of Geodynamics*, **5,** 383–396.

Berberian, M., 1976. Contribution to the seismotectonics of Iran (Part II). *Geological Survey of Iran. Rep. No.*, **39,** 518.

Berberian, F. & Berberian, M., 1981. Tectono-plutonic episodes in Iran. In: *Zagros-Hindu Kush-Himalaya Geodynamic Evolution* (edsGupta, H. & Delany, F.), *American Geophysical Union, Geodynamics Series*, **3:** 5–32.

Berman, R.G., 1988. Internally-consistent thermodynamic data for minerals in the system Na_2O-K_2O-CaO-MgO-FeO-Fe_2O_3-Al_2O_3-SiO_2-TiO_2-H_2O-CO_2. *Journal of Petrology*, **29,** 445–522.

Boulin, J., 1988. Hercynian and Eocimmerian events in Afghanistan and adjoining regions. *Tectonophysics*, **148,** 253–278.

Brookfield, M.E. & Hashmat, A., 2001. The geology and petroleum potential of the North Afghan platform and adjacent areas (northern Afghanistan, with parts of southern Turkmenistan, Uzbekistan and Tajikistan). *Earth Science Reviews*, **55,** 41–71.

Brown, E.H., 1977. The crossite content of Ca-amphibole as a guide to pressure of metamorphism. *Journal of Petrology*, **18,** 53–72.

de Capitani, C. & Brown, T.H., 1987. The computation of chemical equilibrium in complex systems containing non-ideal solutions. *Geochimica et Cosmochimica Acta*, **51,** 2639–2652.

Çetinkaplan, M., Candan, O., Oberhänsli, R. & Bousquet, R., 2008. Pressure-temperature evolution of lawsonite eclogite in Sivrihisar; Tavşanlı Zone-Turkey. *Lithos*, **104,** 12–32.

Charusiri, P., Clark, A.H., Farrar, E., Archibald, D. & Charusiri, B., 1993. Granite belts in Thailand: evidence from the $^{40}Ar/^{39}Ar$ geochronological and geological syntheses. *Journal of Southeast Asian Earth Sciences*, **8,** 127–136.

Clark, G.C., Davies, R.G., Hamzepour, G. & Jones, C.R., 1975. *Explanatory Text of the Bandar-e-Pahlavi Quadrangle Map, 1:250,000*. Geological Survey of Iran, Tehran, Iran, 198 pp.

Colombi, A., 1989. Métamorphisme et géochimie des rocks mafiques des Alpes Ques-centrales (géoprofil Viége-Domodossola-Locarno). *Mémoir Géologie Lausanne*, **4,** 1–216.

Crawford, M.A., 1977. A summary of isotopic age data for Iran, Pakistan and India. In: *Libre a la memoire del A.F. de Lapparent. Mémoire hors-serie 8*, pp. 251–260. Paris, Societé Géologique de France.

Debon, F., Afzali, H., LeFort, P., Sonet, J. & Zimmermann, J.L., 1987. Plutonic rocks and associations in Afghanistan: typology, age and geodynamic setting. *Memoire Science de la Terre, Nancy*, **49,** 132.

Dercourt, J., Ricou, L.E. & Vrielynk, B., 1993. *Atlas Tethys Paleoenvironmental Maps*. Editions Gauthier-Villars, Paris, 307 pp.

Ellis, D.J. & Green, D.H., 1979. An experimental study of the effect of Ca upon garnet-clinopyroxene Fe-Mg exchange equilibria. *Contributions to Mineralogy and Petrology*, **71,** 13–22.

Evans, B.W., 1990. Phase relation of epidote-blueschist. *Lithos*, **25,** 3–23.

Fitzherbert, J.A., Clarke, G.L. & Powell, R., 2005. Preferential retrogression of high -*P* metasediments and the preservation of blueschist to eclogite facies metabasite during exhumation, Diahot terrane, NE New Caledonia. *Lithos*, **83,** 67–96.

Floyd, P.A. & Winchester, J.A., 1975. Magma type and tectonic setting discrimination using immobile elements. *Earth and Planetary Science Letters*, **27,** 211–218.

Franz, G. & Selverstone, J., 1992. An empirical phase diagram for the clinozoisite-zoisite transformation in the system $Ca_2Al_3Si_3O_{12}(OH)$-$Ca_2Al_2Fe^{3+}Si1_2(OH)$. *American Mineralogist*, **77,** 631–642.

Gaetani, M., 1997. The Karakorum Block in Central Asia, from Ordovician to Cretaceous. *Sedimentary Geology*, **109,** 339–359.

Galoyan, G.H., Rolland, Y., Sosson, M. *et al.*, 2009. Geology, geochemistry and $^{40}Ar/^{39}Ar$ dating of Sevan ophiolites (Lesser Caucasus, Armenia): evidence for Jurassic Back-arc opening and hot spot event between the South Armenian Block and Eurasia. *Journal of Asian Earth Sciences*, **34,** 135–153.

Gamkrelidze, I.P. & Shengelia, D.M., 2007. Pre-Alpine geodynamics of the Caucasus, suprasubduction, regional metamorphism and granitoid magmatism. *Bulletin of the Georgian National Academy of Sciences*, **175,** 21.

Garzanti, E. & Gaetani, M., 2002. Unroofing history of Late Palaeozoic magmatic arcs within the "Turan Plate" (Tuarkyr, Turkmenistan). *Sedimentary Geology*, **151,** 67–87.

Gu, L., Du, J., Zhai, J., Fan, J., Zhao, C. & Zhang, W., 2002. Composition of Phengites in Eclogites and their Retrogressive Derivatives of the Dabieshan Region: implication for the Applicability of Phengite Geobarometre. *Chinese Journal of Geochemistry*, **21,** 52–56.

Hennig, D., Lehmann, B., Frei, D. *et al.*, 2009. Early Permian seafloor to continental arc magmatism in the eastern Paleo--Tethys: U-Pb age and Nd-Sr isotope data from the southern Lancangjiang zone, Yunnan, China. *Lithos*, **113,** 408–422.

Holland, T.J.B., 1979. High water activities in the generation of high pressure kyanite eclogite in the Tauern Window, Austria. *Journal of Geology*, **87,** 1–27.

Holland, T.J.B., 1980. The reaction albite=jadeite + quartz determined experimentally in the range 600–1200°C. *American Mineralogist*, **65,** 129–134.

Holland, T.J.B., 1983. Experimental determination of activities in disordered and short-range ordered jadeitic pyroxenes. *Contributions to Mineralogy and Petrology*, **82,** 214–220.
Isozaki, Y., Aoki, K., Nakama, T. & Yanai, S., 2010. New insight into a subduction-related orogen: a reappraisal of the geotectonic framework and evolution of the Japanese Islands. *Gondwana Research*, **18,** 82–105.
Jassim, S.Z. & Goff, J., 2006. *Geology of Iraq*. Dolin, Prague and Moravian Museum, Burno.
Kamata, Y., Ueno, K., Hara, H. *et al*., 2009. Classification of the Sibumasu and Paleo-Tethys tectonic division in Thailand using chert lithofacies. *The Island Arc*, **18,** 21–31.
Kapp, P., Yin, A., Manning, C.E., Harrison, T.M. & Taylor, M.H., 2003. Tectonic evolution of the early Mesozoic blueschist-bearing metamorphic belt, central Tibet. *Tectonics*, **24,** 1043.
Kazmin, V.G., Sbortshikov, I.M., Ricou, L-E., Zonenshain, L.P., Boulin, L. & Knipper, A.L., 1986. Volcanic belts as markers of the Mesozoic-Cenozoic active margin of Eurasia, *Tectonophysics*, **123,** 123–152.
Konstantinovskaia, E.A., Brunel, M. & Malavieille, J., 2003. Discovery of the Paleo-Tethys residual peridotites along the Anyemaqen-KunLun suture zone (North Tibet). *Comptes Rendus Geoscience*, **335,** 709–719.
Kostka, R., 2002. The world mountain Damavand: documentation and monitoring of human activities using remote sensing data. *ISPRS Journal of Photogrammetry and Remote Sensing*, **57,** 5–12.
Krogh, E.J., 1988. The garnet-clinopyroxene Fe-Mg geothermometer – a reinterpretation of existing experimental data. *Contributions to Mineralogy and Petrology*, **99,** 44–48.
Leake, B.E., 1978. Nomenclature of amphiboles. *Canadian Mineralogist*, **16,** 501–520.
Lemaire, M.M., Westphal, M., Gurevitch, E.L., Nazarov, K., Feinberg, H. & Pozzi, J.P., 1997. How far between Iran and Eurasia was the Turan plate during Triassic-Jurassic times? *Geologie en Mijnbouw*, **76,** 73–82.
Lepvrier, C., Maluski, H., Van Tich, V., Leyreloup, A., Truong Thi, P. & Van Vuong, N., 2004. The Early Triassic Indosinian orogeny in Vietnam (Truong Son Belt and Kontum Massif); implications for the geodynamic evolution of Indochina. *Tectonophysics*, **393,** 87–118.
Liou, J.G., Tsujimori, T., Zhang, R.Y., Katayama, I. & Maruyama, S., 2004. Global UHP metamorphism and continental subduction/collision: the Himalayan model. *International Geology Review*, **46,** 1–27.
Liu, C., Mo, X., Luo, Z. *et al*., 2004. Mixing events between the crust-and mantle-derived magmas in Eastern Kunlun: evidence from zircon SHRIMP-chronology. *Chinese Science Bulletin*, **49,** 828–834.
Majidi, B., 1978. *Etude pérostructurale de la région de Mashad (Iran). Les problèmes des méamorphites, serpentinites et granitoides hercyniens*. Thèse de Docteur Ingenieur, Université Scientifique e Médicale de Grenoble, Grenoble, France, 277 pp.
Maruyama, S., Cho, M. & Liou, J.G. 1986. Experimental investigations of blueschist-greenschist transition equilibria: pressure dependence of Al_2O_3 contents in sodic amphiboles-a new geobarometer. In: *Geological Society of America, Memoir* (eds Evans, B.W. & Brown, E.H.), 1–6. Boulder, CO. Blueschists and Eclogites. 164
Mattern, F. & Schneider, W., 2000. Suturing of the Proto- and Paleo-Tethys oceans in the western Kunlun (Xinjiang, China). *Journal of Asian Earth Sciences*, **18,** 637–650.
Moazzen, M., Omrani, H., Oberhänsli, R., Moayyed, M., Tsujimori, T. & Bousquet, R., 2010. *Shanderman Eclogites from Northern Iran, P-T Path and Paleotethys Geodynamics from Subduction to Exhumation*. METU (Middle East Technical University). Ankara, Turkey. Abstracts, Tectonic Crossroads: Evolving Orogens of Eurasia-Africa Arabia. GSA meeting, METU of Ankara, 4-8 Oct. 2010.
Moix, P., Beccaletto, L., Kozur, H.W., Hochard, C., Rosselet, F. & Stampfli, G.M., 2008. A new classification of the Turkish terranes and sutures and its implication for the paleotectonic history of the region. *Tectonophysics*, **451,** 7–39.
Morimoto, N., Fabries, J., Ferguson, A.K. *et al*., 1988. Nomenclature of pyroxenes. *Mineralogical Magazine*, **52,** 535–550.
Natal'in, B.A. & Şengör, A.M.C., 2005. Late Palaeozoic to Triassic evolution of the Turan and Scythian platforms: the pre-history of the Palaeo-Tethyan closure. *Tectonophysics*, **404,** 175–202.
Nazari, H., Omrani, J., Shahidi, A., Salamati, R. & Moosavi, A., 2004. *Geological Map of Bandar-e- Anzali, 1:100,000*. Geological Survey of Iran, Tehran, Iran.
Nishimura, Y., 1998. Geotectonic subdivision and areal extent of the Sangun belt, inner zone of Southwest Japan. *Journal of Metamorphic Geology*, **16,** 129–140.
O'Brien, P.J., Zotov, N., Law, R., Khan, M.A. & Jan, M.Q., 2001. Coesite in Himalayan eclogite and implications for models of India-Asia collision. *Geology*, **29,** 435–438.
Okay, A., 1989. Alpine-Himalayan blueschists. *Annual Review of Earth and Planetary Sciences*, **17,** 55–87.
Okay, A.I. & Whitney, D.L., 2010. Blueschist, eclogites, ophiolites and suture zones in northern Turkey: a review and a field excursion guide. *Ofioliti*, **35,** 131–172.
Okay, A., Harris, N.B.W. & Kelley, S.P., 1998. Exhumation of blueschists along the Tethyan suture in northwest Turkey. *Tectonophysics*, **285,** 275–299.
Okay, A.I., Monod, O. & Monié, P., 2002. Triassic blueschists and eclogites from northwest Turkey: vestiges of the Paleo-Tethyan subduction. *Lithos*, **64,** 155–178.
Omrani, H., Moayyed, M., Oberhänsli, R., Bousquet, R. & Tsujimori, T., 2009. Geochemistry of Shanderman eclogites and their protolith nature. *Iranian Journal of Crystallography and Mineralogy*, **89,** 431–444.
Poli, S. & Schmidt, M.W., 1995. H_2O transport and release in subduction zones: experimental constraints on basaltic and andesitic systems. *Journal of Geophysical Research*, **100,** 22299–22314.
Powell, R., 1985. Regression diagnostics and robust regression in geothermometer / geobarometer calibration: the garnet-clinopyroxene geothermometer revisited. *Journal of Metamorphic Geology*, **3,** 231–243.
Radvanec, M., Banno, S. & Okamoto, K., 1994. Multiple stages of phengite formation in Sanbagawa schists. *Mineralogy and Petrology*, **51,** 37–48.
Räheim, A. & Green, D.H., 1974. Experimental determination of the temperature and pressure dependence of the Fe-Mg partition coefficient for coexisting garnet and clinopyroxene. *Contributions to Mineralogy and Petrology*, **48,** 179–203.
Roger, F., Jolivet, M. & Malavieille, J., 2008. Tectonic evolution of the Triassic fold belts of Tibet. *Comptes Rendus Geoscience*, **340,** 180–189.
Rolland, Y., Galoyan, G.H., Bosch, D. *et al*., 2009a. Jurassic Back-arc and hot-spot related series in the Armenian ophiolites – implications for the obduction process. *Lithos*, **112,** 163–187.
Rolland, Y., Billo, S., Corsini, M., Sasson, M. & Galoyan, G., 2009b. Blueschists of the Amassia-Stepanavan suture zone (Armenia): linking Tethys subduction history from E-Turkey to W-Iran. *International Journal of Earth Sciences*, **98,** 533–550.
Rolland, Y., Sosson, M., Adamia, S.H. & Sadradze, N., 2011. Prolonged 'Variscan to Alpine' history of Active Eurasian margin (Georgia, Armenia) revealed by $^{40}Ar/^{39}Ar$ dating. *Gondwana Research*, **20,** 798–815.
Ruban, D.A., AL-Husseini, M.I. & Iwasaki, Y., 2007. Review of Middle East Palaeozoic plate tectonics. *GeoArabia* **12,** 35–56.
Şengör, A.M.C., 1979. Mid-Mesozoic closure of Permo-Triassic Tethys and its implications. *Nature*, **279,** 590–593.

Şengör, A.M.C., 1990. A new model for the late Palaeozoic-Mesozoic tectonic evolution of Iran and implications for Oman. *Geological Society of London, Special Publications*, **49,** 797–831.

Şengör, A.M.C., 1992. The Palaeo-Tethyan suture: a line of demarcation between two fundamentally different architectural styles in the structure of Asia. *The Island Arc*, **1,** 78–91.

Seyed-Emami, K., Fürsich, F.T., Wilmsen, M. *et al*., 2006. Stratigraphy and ammonite fauna of the upper Shemshak Formation (Toarcian-Aalenian) at Tazareh, eastern Alborz. Iran. *Journal of Asian Earth Sciences*, **28,** 259–275.

Shervais, J.W., 1982. Ti-V plots and the petrogenesis of modern and ophiolitic lavas. *Earth and Planetary Science Letters*, **59,** 101–118.

Sone, M. & Metcalfe, I., 2008. Parallel Tethyan sutures in mainland Southeast Asia: new insights for Palaeo-Tethys closure and implications for the Indosinian orogeny. *Comptes Rendus Geoscience*, **340,** 166–179.

Stampfli, G.M. & Borel, G.D., 2002. A plate tectonic model for the Palaeozoic and Mesozoic constrained by dynamic plate boundaries and restored synthetic oceanic isochrones. *Earth and Planetary Science Letters*, **196,** 17–33.

Stampfli, G.M. & Kozur, H.W., 2006. Europe from the Variscan to the Alpine cycles. In: *European Lithosphere Dynamics* (eds Gee, D.G. & Stephenson, R.A.), *Memoir of the Geological Society of London*, **32,** 57–82.

Stampfli, G.M., von Raumer, J.F. & Borel, G.D., 2002. Palaeozoic evolution of pre-Variscan terranes: from Gondwana to the Variscan collision. In: *Variscan-Appalachian Dynamics: The Building of the Late Palaeozoic Basement* (eds Martínez Catalán, J.R., Hatcher, R.D. Jr, Arenas, R. & Díaz García, F.), pp. 263–280. Boulder, CO. Geological Society of America Special Paper.

Stöcklin, J., 1974. Possible Ancient Continental Margin in Iran. In: *The Geology of Continental Margins* (eds Burk, C.A. & Drake, C.L.), pp. 873–887. Berlin, Springer.

Tikhomirov, P.L., Chalot-Prat, F. & Nazarevich, B.P., 2004. Triassic volcanism in the Eastern Fore-Caucasus: evolution and geodynamic interpretation. *Tectonophysics*, **381,** 119–142.

Tropper, E. & Manning, C.E., 2004. Paragonite stability at 700°C in the presence of H_2O-NaCl fluids: constraints on H_2O activity and implications for high pressure metamorphism. *Contributions to Mineralogy and Petrology*, **147,** 740–749.

Tsai, C.H. & Liou, J.G., 2000. Eclogite-facies relics and inferred ultrahigh-pressure metamorphism in the North Dabie Complex, central-eastern China. *American Mineralogist*, **85,** 1–8.

Tsujimori, T., 2002. Prograde and retrograde P-T paths of the late Palaeozoic glaucophane eclogite from the Renge metamorphic belt, Hida Mountains, southwestern Japan. *International Geology Review*, **44,** 797–818.

Tsujimori, T. & Itaya, T., 1999. Blueschist-facies metamorphism during Palaeozoic orogeny in southwestern Japan: Phengite K-Ar ages of blueschist-facies tectonic blocks in a serpentinite mélange beneath early Palaeozoic Oeyama ophiolite. *The Island Arc*, **8,** 190–205.

Tsujimori, T., Tanaka, C., Sakurai, T. *et al*., 2000. Illustrated introduction to Eclogite in Japan. *Bulletin of Research Institute of Natural Sciences, Okayama University of Science*, **26,** 19–27.

Tsujimori, T., Sisson, V.B., Liou, J.G., Harlow, G.E. & Sorensen, S.S., 2006. Petrologic characterization of Guatemalan lawsonite eclogite: Eclogitization of subducted oceanic crust in a cold subduction zone. *Geological Society of America Special Paper*, **403,** 147–168.

Vernant, P., Nilforoushan, F., Chery, J. *et al*., 2004. Deciphering oblique shortening of central Alborz in Iran using geodetic data. *Earth and Planetary Science Letters*, **223,** 177–185.

Weislogel, A.L., 2008. Tectonostratigraphic and geochronologic constraints on evolution of the northeast Paleotethys from the Songpan-Ganzi complex, central China. *Tectonophysics*, **451,** 331–345.

White, R.W., Powell, R., Holland, T.J.B. & Worley, B.A., 2000. The effect of TiO_2 and Fe_2O_3 on metapelitic assemblages at greenschist and amphibolite facies conditions; mineral equilibria calculations in the system K_2O–FeO–MgO–Al_2O_3–SiO_2–H_2O–Fe_2O_3 *Journal of Metamorphic Geology*, **18,** 497–511.

Whitney, D.L. & Davis, P.B., 2006. Why is lawsonite eclogite so rare? Metamorphism and preservation of lawsonite eclogite, Sivrihisar, Turkey. *Geology*, **34,** 473–476.

Whitney, D.L., Evans, B.W. 2010. Abbreviations for names of rock-forming minerals. *American Mineralogist*, **95,** 185–187.

Whitney, D.L., Teyssier, C., Toraman, E., Seaton, N.C.A. & Fayon, A.K., 2011. Metamorphic and tectonic evolution of a structurally continuous blueschist-to-Barrovian terrane, Sivrihisar Massif, Turkey. *Journal of Metamorphic Geology*, **29,** 193–212.

Winchester, J.A. & Floyd, P.A., 1977. Geochemical discrimination of different magma series and their differentiation products using immobile elements. *Chemical Geology*, **20,** 325–343.

Wintsch, R.P., Byrne, T. & Toriumpi, M., 1999. Exhumation of the Sanbagawa blueschist belt, SW Japan, by lateral flow and extrusion: evidence from structural kinematics and retrograde P-T-t paths. *Geological Society of London Special Publications*, **154,** 129–155.

Xiao, L., Zhang, H.F., Clemens, J.D. *et al*., 2007. Late Triassic granitoids of the eastern margin of the Tibetan Plateau: geochronology, petrogenesis and implications for tectonic. *Lithos*, **96,** 436–452.

Xu, R., Zhang, Y., Vidal, P. & Arnaud, N., 1992. *Two Plutonic Belts in Western Kunlun*. Kashi, Xinjiang, China, 62 pp. International Symposium on the Karakorum and Kunlun Mountains. Abstracts.

Yang, J., Xu, Z., Li, Z. *et al*., 2009. Discovery of an eclogite belt in the Lhasa block, Tibet: a new border for Paleo-Tethys? *Journal of Asian Earth Sciences*, **34,** 76–89.

Yokoyama, K., Brothers, R.N. & Black, P.M., 1986. Regional eclogite facies in the high-pressure metamorphic belt of New Caledonia. *Geological Society of America, Memoir*, **164,** 407–423.

Zanchetta, S., Zanchi, A., Villa, I., Poli, S. & Muttoni, G., 2009. The Shanderman eclogites: a Late Carboniferous high-pressure event in the NW Talesh Mountains (NW Iran). *Geological Society of London, Special Publications*, **312,** 57–78.

Zanchi, A., Berra, F., Mattei, M., Ghassemi, R.M. & Sabouri, J., 2006. Inversion tectonics in central Alborz, Iran. *Journal of Structural Geology*, **28,** 2023–2037.

Zhang, Y., Xie, Y., Xu, R., Vidal, P. & Arnaud, N., 1992. *Elements Geochemistry of Granitoid Rocks in the West Qinghai-Xizang Plateau*. Kashi, Xinjiang, China, 64 pp. International Symposium on the Karakorum and Kunlun Mountains. Abstracts.

Zhang, Q., Wang, C.Y., Liu, D. *et al*., 2008. A brief review of ophiolites in China. *Journal of Asian Earth Sciences*, **32,** 308–324.

Received 20 June 2012; revision accepted 24 June 2013.